



HAL
open science

A loosely coupled scheme for fictitious domain approximations of fluid-structure interaction problems with immersed thin-walled structures

Ludovic Boilevin-Kayl, Miguel Angel Fernández, Jean-Frédéric Gerbeau

► To cite this version:

Ludovic Boilevin-Kayl, Miguel Angel Fernández, Jean-Frédéric Gerbeau. A loosely coupled scheme for fictitious domain approximations of fluid-structure interaction problems with immersed thin-walled structures. *SIAM Journal on Scientific Computing*, 2019, 41 (2), pp.351-374. 10.1137/18M1192779 . hal-01811290v2

HAL Id: hal-01811290

<https://inria.hal.science/hal-01811290v2>

Submitted on 26 Mar 2019

HAL is a multi-disciplinary open access archive for the deposit and dissemination of scientific research documents, whether they are published or not. The documents may come from teaching and research institutions in France or abroad, or from public or private research centers.

L'archive ouverte pluridisciplinaire **HAL**, est destinée au dépôt et à la diffusion de documents scientifiques de niveau recherche, publiés ou non, émanant des établissements d'enseignement et de recherche français ou étrangers, des laboratoires publics ou privés.

3 **A LOOSELY COUPLED SCHEME FOR FICTITIOUS DOMAIN**
4 **APPROXIMATIONS OF FLUID-STRUCTURE INTERACTION**
5 **PROBLEMS WITH IMMERSSED THIN-WALLED STRUCTURES***

6 LUDOVIC BOILEVIN-KAYL[†], MIGUEL A. FERNÁNDEZ[†],
7 AND JEAN-FRÉDÉRIC GERBEAU[†]

8 **Abstract.** Fictitious domain approximations of fluid-structure interaction problems are gener-
9 ally discretized in time using strongly coupled schemes. This guarantees unconditional stability but
10 at the price of solving a computationally demanding coupled system at each time-step. The design of
11 loosely coupled schemes (i.e., methods that invoke the fluid and solid solvers only once per time-step)
12 is of fundamental interest, especially for three-dimensional simulations, but the existing approaches
13 are known to suffer from severe stability and/or time accuracy issues. We propose a new approach
14 that overcomes these difficulties in the case of the coupling with immersed thin-walled structures.

15 **Key words.** fluid-structure interaction, incompressible fluid, immersed thin-walled structure,
16 unfitted meshes, fictitious domain method, coupling schemes

17 **AMS subject classifications.** 65M85, 74F10, 76M10

18 **DOI.** 10.1137/18M1192779

19 **1. Introduction.** One of the main difficulties that have to be faced when solving
20 incompressible fluid-structure interaction problems are the numerical issues related to
21 the added-mass effect (see, e.g., [39, 17, 27, 49]). This difficulty has been traditionally
22 overcome by considering *strongly coupled* schemes, in which the interface conditions
23 are treated in a fully implicit fashion. This ensures stability and time accuracy but at
24 the price of solving a heterogeneous ill-conditioned system at each time-step, which
25 can be computationally demanding in practice.

26 Over the last decade, significant advances have been achieved in the development
27 and in the analysis of fluid-solid splitting schemes that avoid strong coupling, without
28 compromising stability and accuracy. In the majority of these studies, the spatial
29 discretization is based on body fitted fluid meshes (see, e.g., [21, 44, 5, 14, 31, 13,
30 20, 25, 6, 26, 23, 38]). Fitted meshes are very appealing because they facilitate the
31 accurate prescription of the interface conditions. However, this framework rapidly
32 becomes cumbersome or unfeasible in the presence of large interface deflections or of
33 topological changes (e.g., due to contact between solids). In this case, the alternative
34 is to consider an unfitted mesh formulation, in which the fluid mesh is independent
35 of the solid mesh (see, e.g., [43, 40, 51, 28, 45, 18, 3, 9, 15, 34, 10, 1, 33]).

36 Within the unfitted mesh framework, splitting schemes which avoid strong cou-
37 pling are rare in the literature. In fact, we are only aware of the methods reported in
38 [9, 2, 36], using immersed boundary or fictitious domain methods, and in [15, 1, 33],
39 using unfitted Nitsche based methods with cut-elements. The fundamental drawback
40 of the *loosely coupled* (or *explicit coupling*) schemes, reported in [9, 15, 33, 36], is

*Submitted to the journal’s Computational Methods in Science and Engineering section June 11,
2018; accepted for publication (in revised form) February 13, 2019; published electronically DATE.
<http://www.siam.org/journals/sisc/x-x/M119277.html>

Funding: This work was supported by the project MIVANA, a collaborative project for the
development of new technologies for mitral valve repair, which was led by the start-up company
Kephalios, with the participation of the start-up company Epygon, who received funds from the
French government, in the context of the program “Investissement d’Avenir.”

[†]Inria Paris, 75012 Paris, France and Sorbonne Université, UMR 7598 LJLL, 75005 Paris, France
(ludovic.boilevin-kayl@inria.fr, miguel.fernandez@inria.fr, jean-frederic.gerbeau@inria.fr).

41 that their stability/accuracy demands severe time-step restrictions or is limited by
 42 the amount of added-mass effect. These issues have been recently circumvented in
 43 [1, 2], by borrowing the ideas from [20], but at the price of compromising the explicit
 44 nature of the coupling scheme. Indeed, the resulting methods are only *semi-implicit*
 45 (see also [22]).

46 In this paper, we introduce and analyze a new loosely coupled scheme for fictitious
 47 domain approximations of fluid-structure interaction problems with immersed thin-
 48 walled structures that overcomes the above mentioned issues. Our starting point is the
 49 semi-implicit coupling scheme reported in [2]. We show that the combination of an ap-
 50 propriate choice of the Lagrange multipliers space (equivalent to a *collocation method*)
 51 with a mass lumping approximation in the solid yield a loosely coupled scheme. We
 52 also present a general stability result that proves that the scheme is unconditionally
 53 stable in the energy norm. Numerical experiments in a series of representative two-
 54 dimensional examples, involving large interface deflections and topology changes in
 55 the fluid domain, illustrate the performance of the proposed approach.

56 The rest of the paper is organized as follows. Section 2 presents the coupled
 57 problem considered through the paper. The fictitious domain spatial approximation
 58 is introduced in section 3. Section 4 presents the new coupling scheme and its stability
 59 analysis. The numerical experiments are reported in section 5. Finally, a summary of
 60 the main results obtained with some lines of future research are drawn in section 6.

62 **2. Problem setting.** We consider a fluid-structure interaction problem in which
 63 the fluid is described by the incompressible Navier–Stokes equations and the struc-
 64 ture by a thin-walled solid model (curved beam in two dimensions or shell in three
 65 dimensions). Let $\Sigma \subset \mathbb{R}^d$ be the reference configuration of the solid mid-surface
 66 ($d = 2, 3$). The current position of the interface, denoted by $\Sigma(t)$, is parameter-
 67 ized by its motion map $\phi : \Sigma \times \mathbb{R}^+ \rightarrow \mathbb{R}^d$ as $\Sigma(t) = \phi(\Sigma, t)$, with $\phi \stackrel{\text{def}}{=} \mathbf{I}_\Sigma + \mathbf{d}$,
 68 where \mathbf{d} denotes the displacement of the solid. In order to ease the presentation, we
 69 introduce the notation $\phi_t \stackrel{\text{def}}{=} \phi(\cdot, t)$, so that we also have $\Sigma(t) = \phi_t(\Sigma)$. The struc-
 70 ture is supposed to move within a domain $\Omega \subset \mathbb{R}^d$ with boundary $\Gamma \stackrel{\text{def}}{=} \partial\Omega$ (see
 71 Figure 1). For simplicity and without loss of generality, Ω is assumed to be fixed.
 72 The fluid is described in the time-dependent control volume $\Omega(t) \stackrel{\text{def}}{=} \Omega \setminus \Sigma(t) \subset \mathbb{R}^d$,
 73 with its boundary partitioned as $\partial\Omega(t) = \Sigma(t) \cup \Gamma$. The interface $\Sigma(t)$ is assumed
 74 to be oriented by a unit normal vector field denoted by \mathbf{n}^s . This induces a posi-
 75 tive and a negative side in the fluid domain $\Omega(t)$, with respective unit normals
 76 $\mathbf{n}^+ \stackrel{\text{def}}{=} \mathbf{n}^s$ and $\mathbf{n}^- \stackrel{\text{def}}{=} -\mathbf{n}^s$ on $\Sigma(t)$. For a given continuous scalar or tensorial
 77 field f defined in $\Omega(t)$ (possibly discontinuous across the interface $\Sigma(t)$), we define

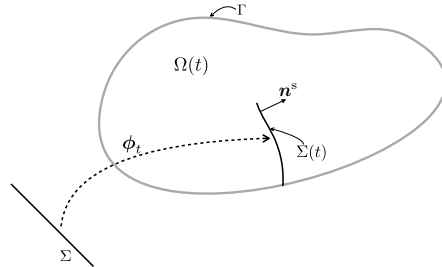


FIG. 1. Geometric description.

78 its positive and negative sided-restrictions to $\Sigma(t)$, denoted respectively by f^+ and
 79 f^- , as $f^+(\mathbf{x}) \stackrel{\text{def}}{=} \lim_{\xi \rightarrow 0^+} f(\mathbf{x} + \xi \mathbf{n}^+)$, $f^-(\mathbf{x}) \stackrel{\text{def}}{=} \lim_{\xi \rightarrow 0^+} f(\mathbf{x} + \xi \mathbf{n}^-)$ for all $\mathbf{x} \in \Sigma(t)$.
 80 We shall also make use of the following jump operators across the interface $\Sigma(t)$:
 81 $[[f]] \stackrel{\text{def}}{=} f^+ - f^-$, $[[f\mathbf{n}]] \stackrel{\text{def}}{=} f^+ \mathbf{n}^+ + f^- \mathbf{n}^-$.

82 The considered nonlinear coupled problem reads as follows: find the fluid velocity
 83 and pressure $\mathbf{u} : \Omega \times \mathbb{R}^+ \rightarrow \mathbb{R}^d$, $p : \Omega \times \mathbb{R}^+ \rightarrow \mathbb{R}$ and the solid displacement and
 84 velocity $\mathbf{d} : \Sigma \times \mathbb{R}^+ \rightarrow \mathbb{R}^d$, $\dot{\mathbf{d}} : \Sigma \times \mathbb{R}^+ \rightarrow \mathbb{R}^d$ such that

$$(2.1) \quad \begin{cases} \rho^f (\partial_t \mathbf{u} + \mathbf{u} \cdot \nabla \mathbf{u}) - \text{div} \boldsymbol{\sigma}(\mathbf{u}, p) = \mathbf{0} & \text{in } \Omega(t), \\ \text{div} \mathbf{u} = 0 & \text{in } \Omega(t), \\ \mathbf{u} = \mathbf{0} & \text{on } \Gamma, \end{cases}$$

$$(2.2) \quad \begin{cases} \rho^s \epsilon^s \partial_t \dot{\mathbf{d}} + \mathbf{L} \mathbf{d} = \mathbf{T} & \text{on } \Sigma, \\ \dot{\mathbf{d}} = \partial_t \mathbf{d} & \text{on } \Sigma, \end{cases}$$

$$(2.3) \quad \begin{cases} \phi = \mathbf{I}_\Sigma + \mathbf{d}, \quad \Sigma(t) = \phi(\Sigma, t), \quad \Omega(t) = \Omega \setminus \Sigma(t), \\ \mathbf{u} = \dot{\mathbf{d}} \circ \phi_t^{-1} & \text{on } \Sigma(t), \\ \int_\Sigma \mathbf{T} \cdot \mathbf{w} = - \int_{\Sigma(t)} [[\boldsymbol{\sigma}(\mathbf{u}, p) \mathbf{n}]] \cdot \mathbf{w} \circ \phi_t^{-1} \end{cases}$$

91 for all smooth test functions $\mathbf{w} : \Sigma \rightarrow \mathbb{R}^d$. The above coupled system has to be
 92 complemented with appropriate initial conditions $\mathbf{u}(0) = \mathbf{u}_0$, $\mathbf{d}(0) = \mathbf{d}_0$ and $\dot{\mathbf{d}}(0) = \dot{\mathbf{d}}_0$.
 93 Here, ρ^f and ρ^s respectively denote the fluid and solid densities, ϵ^s the thickness of
 94 the solid, and the fluid Cauchy stress tensor is given by

$$(95) \quad \boldsymbol{\sigma}(\mathbf{u}, p) \stackrel{\text{def}}{=} 2\mu \boldsymbol{\epsilon}(\mathbf{u}) - p \mathbf{I}, \quad \boldsymbol{\epsilon}(\mathbf{u}) \stackrel{\text{def}}{=} \frac{1}{2} (\nabla \mathbf{u} + \nabla \mathbf{u}^T),$$

96 where μ denotes the fluid dynamic viscosity. The symbol \mathbf{T} is the force applied
 97 to the structure whereas the symbol \mathbf{L} represents an abstract surface differential
 98 operator that describes the (possibly nonlinear) elastic behavior of the structure. The
 99 three relations in (2.3) enforce, respectively, the geometric, kinematic, and dynamic
 100 interface coupling conditions. Note that the midsurface of the solid is identified with
 101 the fluid-structure interface, by neglecting all the solid thickness effects in the interface
 102 coupling.

103 **3. Weak form with Lagrange multipliers and spatial discretization.** In
 104 what follows, the closed subspaces $H_\Gamma^1(\omega)$, of functions in $H^1(\omega)$ with zero trace on
 105 Γ , and $L_0^2(\omega)$, of functions in $L^2(\omega)$ with zero mean in ω , will be used. The scalar
 106 product in $L^2(\omega)$ is denoted by $(\cdot, \cdot)_\omega$, and we set $(\cdot, \cdot) \stackrel{\text{def}}{=} (\cdot, \cdot)_\Omega$.

107 We consider $\mathbf{V} \stackrel{\text{def}}{=} [H_\Gamma^1(\Omega)]^d$ and $Q \stackrel{\text{def}}{=} L_0^2(\Omega)$ as the fluid velocity and pressure
 108 functional spaces, respectively. The standard Navier–Stokes trilinear form

$$(109) \quad a^f(\mathbf{z}; (\mathbf{u}, p), (\mathbf{v}, q)) \stackrel{\text{def}}{=} \rho^f (\mathbf{z} \cdot \nabla \mathbf{u}, \mathbf{v}) + 2\mu (\boldsymbol{\epsilon}(\mathbf{u}), \boldsymbol{\epsilon}(\mathbf{v})) - (p, \text{div} \mathbf{v}) + (q, \text{div} \mathbf{u})$$

111 will also be used. The space of solid admissible displacements is denoted by $\mathbf{W} \subset$
 112 $[H^1(\Sigma)]^d$. The weak form of the solid elastic operator \mathbf{L} will be represented by an
 113 application $a^s : \mathbf{W} \times \mathbf{W} \rightarrow \mathbb{R}$, which is assumed to be linear only with respect to the
 114 second argument.

$$(3.6) \quad \lambda_C = 1 \quad \text{in} \quad \Omega, \quad \lambda_M = \begin{cases} 1 & \text{in} \quad \Omega \setminus \omega_h^n, \\ \varepsilon_M & \text{in} \quad \omega_h^n, \end{cases}$$

where $0 < \varepsilon_M \ll 1$ is a user-defined (dimensionless) parameter and ω_h^n a neighborhood of the interface Σ_h^n (typically two layers of fluid elements on each of its side). The motivation of the first choice is that it improves local mass conservation while the second reduces the impact of the local residual inconsistencies near the interface.

The solid displacement and velocity are approximated in $\mathbf{W}_h \stackrel{\text{def}}{=} [X_h^s]^d \cap \mathbf{W}$. For the approximation of the Lagrange multiplier, we consider the following nonconforming approximation space (see, e.g., [8, 18, 30, 19]):

$$(3.7) \quad \mathbf{\Lambda}_h = \left\{ \boldsymbol{\mu}_h = \sum_{i=1}^{N_h^s} \boldsymbol{\mu}_i \delta_{\mathbf{x}_i^s} \mid \boldsymbol{\mu}_i \in \mathbb{R}^d, \quad i = 1, \dots, N_h^s \right\},$$

where $\{\mathbf{x}_i^s\}_{i=1}^{N_h^s}$ denotes the points of the triangulation \mathcal{T}_h^s and $\delta_{\mathbf{x}_i^s}$ stands for the Dirac's measure at point \mathbf{x}_i^s . For alternative approximation spaces, the reader is referred to [4, 2, 11], for instance. Due to the nonconforming nature of the approximation (3.7), we introduce the discrete bilinear form $b_h : \mathbf{\Lambda}_h \times [C^0(\Sigma)]^d \rightarrow \mathbb{R}$, defined by

$$(3.8) \quad b_h(\boldsymbol{\mu}_h, \mathbf{z}) \stackrel{\text{def}}{=} \sum_{i=1}^{N_h^s} \boldsymbol{\mu}_i \cdot \mathbf{z}(\mathbf{x}_i^s)$$

for all $(\boldsymbol{\mu}_h, \mathbf{z}) \in \mathbf{\Lambda}_h \times [C^0(\Sigma)]^d$. This amounts to enforce the kinematic constraint (2.3)₂ as in a collocation method (see, e.g., [8, 30]). The spatial semidiscrete approximation of (3.2) reads therefore as follows: for $t > 0$, find $(\mathbf{u}_h, p_h, \mathbf{d}_h, \boldsymbol{\lambda}_h) \in \mathbf{V}_h \times Q_h \times \mathbf{W}_h \times \mathbf{\Lambda}_h$, with $\dot{\mathbf{d}}_h = \partial_t \mathbf{d}_h$, $\boldsymbol{\phi}_h = \mathbf{I}_\Sigma + \mathbf{d}_h$ and such that

$$(3.9) \quad \begin{aligned} \rho^f (\partial_t \mathbf{u}_h, \mathbf{v}_h) + a_h^f(\mathbf{u}_h; (\mathbf{u}_h, p_h), (\mathbf{v}_h, q_h)) + b_h(\boldsymbol{\lambda}_h, \mathbf{v}_h \circ \boldsymbol{\phi}_h - \mathbf{w}_h) \\ + \rho^s \varepsilon^s (\partial_t \dot{\mathbf{d}}_h, \mathbf{w}_h)_\Sigma + a^s(\mathbf{d}_h, \mathbf{w}_h) - b_h(\boldsymbol{\mu}_h, \mathbf{u}_h \circ \boldsymbol{\phi}_h - \dot{\mathbf{d}}_h) = 0 \end{aligned}$$

for all $(\mathbf{v}_h, q_h, \mathbf{w}_h, \boldsymbol{\mu}_h) \in \mathbf{V}_h \times Q_h \times \mathbf{W}_h \times \mathbf{\Lambda}_h$.

4. Time-discretization: Coupling schemes. This section is devoted to the discretization in time of (3.9). In what follows, the parameter $\tau > 0$ stands for the time-step length and $t_n \stackrel{\text{def}}{=} n\tau$, for $n \in \mathbb{N}$. For a given time-dependent field $x(t)$, the symbol x^n denotes an approximation of $x(t_n)$ and $\partial_\tau x^n \stackrel{\text{def}}{=} (x^n - x^{n-1})/\tau$, the first-order backward difference. For simplicity, we consider a first-order time-discretization of the bulk terms in the fluid and in the solid.

We first introduce the strongly coupled scheme reported in Algorithm 4.1 (see, e.g., [11, 9]). The method implicitly treats the kinematic–dynamic coupling through the Lagrange multiplier, but the geometric coupling is treated in an explicit fashion. This yields unconditional stability but at the price of solving the coupled system (4.3) below at each time-step, which can be costly and cumbersome (e.g., when the fluid and the solid are solved in separate codes).

Owing to (3.8), the discrete kinematic constraint in (4.3) writes

$$(4.1) \quad \mathbf{u}_h^n \circ \boldsymbol{\phi}_h^n(\mathbf{x}_i^s) - \dot{\mathbf{d}}_h^n(\mathbf{x}_i^s) = 0 \quad \forall i = 1, \dots, N_h^s.$$

Algorithm 4.1. Strongly coupled scheme.

For $n \geq 1$,

1. Interface update:

$$\phi_h^n = \mathbf{I}_\Sigma + \mathbf{d}_h^{n-1}.$$

2. Find $(\mathbf{u}_h^n, p_h^n, \mathbf{d}_h^n, \boldsymbol{\lambda}_h^n) \in \mathbf{V}_h \times Q_h \times \mathbf{W}_h \times \boldsymbol{\Lambda}_h$, with $\partial_\tau \mathbf{d}_h^n = \dot{\mathbf{d}}_h^n$, such that

$$(4.3) \quad \begin{aligned} & \rho^f (\partial_\tau \mathbf{u}_h^n, \mathbf{v}_h)_\Omega + a_h^f(\mathbf{u}_h^{n-1}; (\mathbf{u}_h^n, p_h^n), (\mathbf{v}_h, q_h)) + b_h(\boldsymbol{\lambda}_h^n, \mathbf{v}_h \circ \phi_h^n - \mathbf{w}_h) \\ & + \rho^s \varepsilon^s (\partial_\tau \dot{\mathbf{d}}_h^n, \mathbf{w}_h)_\Sigma + a^s(\mathbf{d}_h^n, \mathbf{w}_h) - b_h(\boldsymbol{\mu}_h, \mathbf{u}_h^n \circ \phi_h^n - \dot{\mathbf{d}}_h^n) = 0 \end{aligned}$$

for all $(\mathbf{v}_h, q_h, \mathbf{w}_h, \boldsymbol{\mu}_h) \in \mathbf{V}_h \times Q_h \times \mathbf{W}_h \times \boldsymbol{\Lambda}_h$.

189 This is also equivalent to consider in (4.3) (and in (3.9)) the conforming space of
 190 Lagrange multipliers $\boldsymbol{\Lambda}_h = [X_h^s]^d$ and the discrete bilinear form $b_h(\boldsymbol{\mu}_h, \mathbf{z}) = (\boldsymbol{\mu}_h, \mathbf{z})_{\Sigma, h}$.
 191 The symbol $(\cdot, \cdot)_{\Sigma, h}$ denotes the lumped-mass approximation of the L^2 -inner product
 192 $(\cdot, \cdot)_\Sigma$, namely, the surface integral over Σ is approximated using nodal quadrature.
 193 Note that (4.1) avoids the need for the evaluation of interface integrals with quantities
 194 defined on unfitted meshes. Actually, only localization of the solid nodes within the
 195 fluid mesh is required. Little is known however on the discrete inf-sup conditions guar-
 196 anteeing the existence, uniqueness, and convergence of the approximation provided
 197 by (4.3), for these choices of the Lagrange multipliers spaces.

198 *Remark 4.1.* In this regard, we are only aware of two theoretical results. The
 199 first concerns the convergence analysis reported in [19, section 3.2] for the primal
 200 variable of a saddle-point problem involving the Poisson equation, provided that the
 201 local size of the solid mesh is of the same order as the local size of the fluid mesh.
 202 More recently, a complete analysis is given in [11, section 5] for the choice $\boldsymbol{\Lambda}_h = [X_h^s]^d$
 203 and $b_h(\boldsymbol{\mu}_h, \mathbf{z}) = b(\boldsymbol{\mu}_h, \mathbf{z})$ (i.e., without quadrature approximation of the interface
 204 integral), under the assumption that the fluid mesh is sufficiently refined with respect
 205 to the solid mesh.

206 In other to avoid the lack of inf-sup stability result for (4.3), we follow the penalty
 207 strategy considered in [18] for the computer implementation of Algorithm 4.1, which
 208 consists in relaxing (4.1) to

$$209 \quad (4.2) \quad \mathbf{u}_h^n \circ \phi_h^n(\mathbf{x}_i^s) - \dot{\mathbf{d}}_h^n(\mathbf{x}_i^s) = \varepsilon \boldsymbol{\lambda}_i^n \quad \forall i = 1, \dots, N_h^s,$$

211 where $\varepsilon > 0$ is a small (nondimensionless) parameter. This enables the elimination of
 212 the Lagrange multipliers, with the convenient property of preserving the sparse pat-
 213 tern of the matrix of the fluid problem. The fundamental drawbacks of this approach
 214 lie in the choice of the parameter ε (which needs be tuned depending on the mesh
 215 size; see [12]) and in the ill-conditioning issues induced by the resulting penalty term
 216 in the fluid momentum equation.

217 We now consider the alternative numerical method reported in Algorithm 4.2
 218 that is not strongly coupled and, hence, less computationally demanding than Algo-
 219 rithm 4.1. This scheme, introduced in [2] for a different choice of $\boldsymbol{\Lambda}_h$, extends the
 220 ideas of [20, 1] to the unfitted mesh formulation (3.9). Basically, this scheme treats
 221 implicitly the coupling of the fluid with the solid inertia and explicitly the coupling
 222 with the solid elastic effects. The former guarantees stability (by avoiding the explicit
 223 treatment of the added-mass) while the latter reduces the computational complexity
 224 with respect to Algorithm 4.1.

Algorithm 4.2. Semi-implicit scheme (not strongly coupled).

For $n \geq 1$,

1. Interface update:

$$\phi_h^n = \mathbf{I}_\Sigma + \mathbf{d}_h^{n-1}.$$

2. Fluid with solid inertia step: find $(\mathbf{u}_h^n, p_h^n, \dot{\mathbf{d}}_h^{n-\frac{1}{2}}, \boldsymbol{\lambda}_h^n) \in \mathbf{V}_h \times Q_h \times \mathbf{W}_h \times \boldsymbol{\Lambda}_h$ such that

$$(4.4) \quad \begin{aligned} & \rho^f (\partial_\tau \mathbf{u}_h^n, \mathbf{v}_h) + a_h^f(\mathbf{u}_h^{n-1}; (\mathbf{u}_h^n, p_h^n), (\mathbf{v}_h, q_h)) + b_h(\boldsymbol{\lambda}_h^n, \mathbf{v}_h \circ \phi_h^n - \mathbf{w}_h) \\ & + \frac{\rho^s \epsilon^s}{\tau} (\dot{\mathbf{d}}_h^{n-\frac{1}{2}} - \dot{\mathbf{d}}_h^{n-1}, \mathbf{w}_h)_\Sigma - b_h(\boldsymbol{\mu}_h, \mathbf{u}_h^n \circ \phi_h^n - \dot{\mathbf{d}}_h^{n-\frac{1}{2}}) \\ & = -a^s(\mathbf{d}_h^{n-1}, \mathbf{w}_h) \end{aligned}$$

for all $(\mathbf{v}_h, q_h, \mathbf{w}_h, \boldsymbol{\mu}_h) \in \mathbf{V}_h \times Q_h \times \mathbf{W}_h \times \boldsymbol{\Lambda}_h$.

3. Solid update: find $\mathbf{d}_h^n \in \mathbf{W}_h$, with $\dot{\mathbf{d}}_h^n = \partial_\tau \mathbf{d}_h^n$ such that

$$(4.5) \quad \rho^s \epsilon^s (\partial_\tau \dot{\mathbf{d}}_h^n, \mathbf{w}_h)_\Sigma + a^s(\mathbf{d}_h^n, \mathbf{w}_h) = b_h(\boldsymbol{\lambda}_h^n, \mathbf{w}_h)$$

for all $\mathbf{w}_h \in \mathbf{W}_h$.

225 *Remark 4.2.* Alternative extrapolations (e.g., zeroth or second order) could be
 226 considered for the last term of (4.4), as reported in [20, 1, 2]. Nevertheless, in the
 227 present work, we limit the discussion to first-order extrapolation since it guarantees
 228 both unconditional stability (Theorem 4.9) and first-order time accuracy.

229 Note that Algorithm 4.2 uncouples the computation of the fluid and solid un-
 230 knowns $(\mathbf{u}_h^n, p_h^n, \boldsymbol{\lambda}_h^n)$ and $(\dot{\mathbf{d}}_h^n, \mathbf{d}_h^n)$. The price to pay for this splitting is the introduc-
 231 tion of a new unknown in step (4.4), the so-called intermediate solid velocity $\dot{\mathbf{d}}_h^{n-\frac{1}{2}}$.
 232 Similar difficulties arise in the semi-implicit scheme reported in [1, Algorithm 6] for a
 233 Nitsche-XFEM unfitted mesh method (Lagrange multipliers free).

234 **4.1. A new loosely coupled scheme.** The first fundamental idea of the pre-
 235 sent paper is that, if we choose $\boldsymbol{\Lambda}_h$ as in (3.7), both the intermediate velocity $\dot{\mathbf{d}}_h^{n-\frac{1}{2}}$ and
 236 the Lagrange multiplier $\boldsymbol{\lambda}_h^n$ can be eliminated in terms of the standard fluid unknown
 237 (\mathbf{u}_h^n, p_h^n) . To this purpose, we introduce the *fluid-to-solid* Lagrange interpolation
 238 operator

$$239 \quad \mathbf{B}_h : [C^0(\Sigma)]^d \rightarrow \mathbf{W}_h,$$

240 and we state the following result.

241 **LEMMA 4.3.** *Let the discrete space $\boldsymbol{\Lambda}_h$ be given by (3.7). We have*

$$242 \quad (4.6) \quad b_h(\boldsymbol{\mu}_h, \mathbf{v}_h \circ \phi_h^n) = b_h(\boldsymbol{\mu}_h, \mathbf{B}_h(\mathbf{v}_h \circ \phi_h^n)) \quad \forall \mathbf{v}_h \in \mathbf{V}_h.$$

244 *Furthermore, the relation*

$$245 \quad (4.7) \quad b_h(\boldsymbol{\mu}_h, \mathbf{v}_h \circ \phi_h^n - \mathbf{w}_h) = 0 \quad \forall \boldsymbol{\mu}_h \in \boldsymbol{\Lambda}_h$$

247 *is equivalent to*

$$248 \quad (4.8) \quad \mathbf{w}_h = \mathbf{B}_h(\mathbf{v}_h \circ \phi_h^n).$$

250 *Proof.* From (3.8), we have

$$251 \quad b_h(\boldsymbol{\mu}_h, \mathbf{v}_h \circ \phi_h^n) = \sum_{i=1}^{N_h^s} \boldsymbol{\mu}_i \cdot \mathbf{v}_h(\phi_h^n(\mathbf{x}_i^s)) = \sum_{i=1}^{N_h^s} \boldsymbol{\mu}_i \cdot \mathbf{B}_h(\mathbf{v}_h \circ \phi_h^n)(\mathbf{x}_i^s) \\ = b_h(\boldsymbol{\mu}_h, \mathbf{B}_h(\mathbf{v}_h \circ \phi_h^n)).$$

252 On the other hand, owing to (4.7), we get

$$253 \quad \sum_{i=1}^{N_h^s} \boldsymbol{\mu}_i \cdot (\mathbf{B}_h(\mathbf{v}_h \circ \phi_h^n)(\mathbf{x}_i^s) - \mathbf{w}_h(\mathbf{x}_i^s)) = 0$$

254 for all $\boldsymbol{\mu}_i \in \mathbb{R}^d$, or, equivalently,

$$255 \quad \mathbf{B}_h(\mathbf{v}_h \circ \phi_h^n)(\mathbf{x}_i^s) = \mathbf{w}_h(\mathbf{x}_i^s)$$

256 for $i = 1, \dots, N_h^s$, which yields (4.8) and completes the proof. \square

257 The next result shows that the coupled system (4.4) can be formulated exclusively
258 in terms of a pure fluid problem without additional unknowns.

259 **LEMMA 4.4.** *For $n \geq 1$, let $(\mathbf{u}_h^n, p_h^n, \dot{\mathbf{d}}_h^{n-\frac{1}{2}}, \boldsymbol{\lambda}_h^n) \in \mathbf{V}_h \times Q_h \times \mathbf{W}_h \times \boldsymbol{\Lambda}_h$ be solution
260 of (4.4), then we have:*

- 261 • $\dot{\mathbf{d}}_h^{n-\frac{1}{2}} = \mathbf{B}_h(\mathbf{u}_h^n \circ \phi_h^n)$;
- 262 • $(\mathbf{u}_h^n, p_h^n) \in \mathbf{V}_h \times Q_h$ satisfies

$$263 \quad (4.9) \quad \begin{aligned} & \rho^f(\partial_\tau \mathbf{u}_h^n, \mathbf{v}_h) + a_h^f(\mathbf{u}_h^{n-1}; (\mathbf{u}_h^n, p_h^n), (\mathbf{v}_h, q_h)) \\ & + \frac{\rho^s \epsilon^s}{\tau} (\mathbf{B}_h(\mathbf{u}_h^n \circ \phi_h^n), \mathbf{B}_h(\mathbf{v}_h \circ \phi_h^n))_\Sigma \\ 264 & = \frac{\rho^s \epsilon^s}{\tau} (\dot{\mathbf{d}}_h^{n-1}, \mathbf{B}_h(\mathbf{v}_h \circ \phi_h^n))_\Sigma - a^s(\mathbf{d}_h^{n-1}, \mathbf{B}_h(\mathbf{v}_h \circ \phi_h^n)) \end{aligned}$$

265 for all $(\mathbf{v}_h, q_h) \in \mathbf{V}_h \times Q_h$;

- 266 • $\boldsymbol{\lambda}_h^n \in \boldsymbol{\Lambda}_h$ satisfies

$$267 \quad (4.10) \quad b(\boldsymbol{\lambda}_h^n, \mathbf{w}_h) = \frac{\rho^s \epsilon^s}{\tau} (\mathbf{B}_h(\mathbf{u}_h^n \circ \phi_h^n) - \dot{\mathbf{d}}_h^{n-1}, \mathbf{w}_h)_\Sigma + a^s(\mathbf{d}_h^{n-1}, \mathbf{w}_h)$$

269 for all $\mathbf{w}_h \in \mathbf{W}_h$.

270 The reciprocal also holds.

271 *Proof.* From (4.4) with $(\mathbf{v}_h, q_h, \mathbf{w}_h) = (\mathbf{0}, 0, \mathbf{0})$, we have

$$272 \quad b_h(\boldsymbol{\mu}_h, \mathbf{u}_h^n \circ \phi_h^n - \dot{\mathbf{d}}_h^{n-\frac{1}{2}}) = 0 \quad \forall \boldsymbol{\mu}_h \in \boldsymbol{\Lambda}_h$$

273 and

$$274 \quad \begin{aligned} & \rho^f(\partial_\tau \mathbf{u}_h^n, \mathbf{v}_h) + a_h^f(\mathbf{u}_h^{n-1}; (\mathbf{u}_h^n, p_h^n), (\mathbf{v}_h, q_h)) + b_h(\boldsymbol{\lambda}_h^n, \mathbf{v}_h \circ \phi_h^n - \mathbf{w}_h) \\ 275 & + \frac{\rho^s \epsilon^s}{\tau} (\dot{\mathbf{d}}_h^{n-\frac{1}{2}} - \dot{\mathbf{d}}_h^{n-1}, \mathbf{w}_h)_\Sigma = -a^s(\mathbf{d}_h^{n-1}, \mathbf{w}_h) \end{aligned}$$

277 for all $(\mathbf{v}_h, q_h, \mathbf{w}_h) \in \mathbf{V}_h \times Q_h \times \mathbf{W}_h$. Owing to Lemma 4.3, these relations can
278 respectively be formulated as

$$279 \quad (4.11) \quad \mathbf{B}_h(\mathbf{u}_h^n \circ \phi_h^n) = \dot{\mathbf{d}}_h^{n-\frac{1}{2}}$$

and

$$(4.12) \quad \rho^f (\partial_\tau \mathbf{u}_h^n, \mathbf{v}_h) + a_h^f(\mathbf{u}_h^{n-1}; (\mathbf{u}_h^n, p_h^n), (\mathbf{v}_h, q_h)) + b_h(\boldsymbol{\lambda}_h^n, \mathbf{B}_h(\mathbf{v}_h \circ \boldsymbol{\phi}_h^n) - \mathbf{w}_h) \\ + \frac{\rho^s \epsilon^s}{\tau} (\dot{\mathbf{d}}_h^{n-\frac{1}{2}} - \dot{\mathbf{d}}_h^{n-1}, \mathbf{w}_h)_\Sigma = -a^s(\mathbf{d}_h^{n-1}, \mathbf{w}_h)$$

for all $(\mathbf{v}_h, q_h, \mathbf{w}_h) \in \mathbf{V}_h \times Q_h \times \mathbf{W}_h$. Note that the intermediate solid velocity can be eliminated via (4.11). In order to also eliminate the Lagrange multipliers, we take $\mathbf{w}_h = \mathbf{B}_h(\mathbf{v}_h \circ \boldsymbol{\phi}_h^n)$ in (4.12), which yields (4.9). Finally, the relation (4.10) simply follows from (4.11) and (4.12) with $(\mathbf{v}_h, q_h) = (\mathbf{0}, 0)$.

Conversely, we assume now that (4.9) and (4.10) hold. From (4.10), there follows that

$$b(\boldsymbol{\lambda}_h^n, \mathbf{B}_h(\mathbf{v}_h \circ \boldsymbol{\phi}_h^n) - \mathbf{w}_h) - \frac{\rho^s \epsilon^s}{\tau} (\mathbf{B}_h(\mathbf{u}_h^n \circ \boldsymbol{\phi}_h^n) - \dot{\mathbf{d}}_h^{n-1}, \mathbf{B}_h(\mathbf{v}_h \circ \boldsymbol{\phi}_h^n) - \mathbf{w}_h)_\Sigma \\ = a^s(\mathbf{d}_h^{n-1}, \mathbf{B}_h(\mathbf{v}_h \circ \boldsymbol{\phi}_h^n) - \mathbf{w}_h)$$

for all $(\mathbf{v}_h, \mathbf{w}_h) \in \mathbf{V}_h \times \mathbf{W}_h$. By adding this expression to (4.9), we get

$$\rho^f (\partial_\tau \mathbf{u}_h^n, \mathbf{v}_h) + a_h^f(\mathbf{u}_h^{n-1}; (\mathbf{u}_h^n, p_h^n), (\mathbf{v}_h, q_h)) + b_h(\boldsymbol{\lambda}_h^n, \mathbf{B}_h(\mathbf{v}_h \circ \boldsymbol{\phi}_h^n) - \mathbf{w}_h) \\ + \frac{\rho^s \epsilon^s}{\tau} (\mathbf{B}_h(\mathbf{u}_h^n \circ \boldsymbol{\phi}_h^n) - \dot{\mathbf{d}}_h^{n-1}, \mathbf{w}_h)_\Sigma = -a^s(\mathbf{d}_h^{n-1}, \mathbf{w}_h)$$

for all $(\mathbf{v}_h, q_h, \mathbf{w}_h) \in \mathbf{V}_h \times Q_h \times \mathbf{W}_h$. We finally retrieve (4.4) by setting $\dot{\mathbf{d}}_h^{n-\frac{1}{2}} = \mathbf{B}_h(\mathbf{u}_h^n \circ \boldsymbol{\phi}_h^n)$ and by applying Lemma 4.3. This completes the proof. \square

Remark 4.5. Note that (4.9) is a pure fluid problem, with a specific nonnegative bilinear term acting on the interface. It is therefore well posed. Furthermore, owing to the reciprocal part of Lemma 4.4, (4.4) admits also a unique solution.

Remark 4.6. The system (4.9) can be viewed as a fluid problem with an immersed interface condition that generalizes the Robin-base splitting reported in [20, 25, 37] to the case of unfitted meshes. Alternative interface Robin conditions (as those considered in [41, 31, 13] with fitted meshes) can also be generalized with the present approach.

The fundamental difficulty of (4.9) is that, in general, the interfacial term introduces nonstandard coupling terms in the fluid matrix. Even more, the stencil of the resulting matrix depends on the location of the interface at each time-step. In order to overcome these drawbacks, we propose to replace the canonic L^2 -inner product $(\cdot, \cdot)_\Sigma$ in Algorithm 4.2 by its lumped-mass approximation $(\cdot, \cdot)_{\Sigma, h}$ (see, e.g., [48, Chapter 15]). We can then establish the following result.

LEMMA 4.7. *The term*

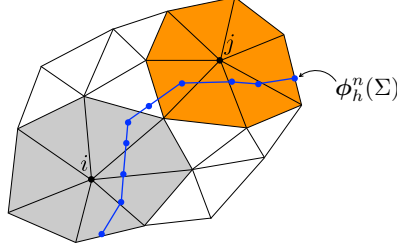
$$(4.13) \quad (\mathbf{B}_h(\mathbf{u}_h^n \circ \boldsymbol{\phi}_h^n), \mathbf{B}_h(\mathbf{v}_h \circ \boldsymbol{\phi}_h^n))_{\Sigma, h}$$

preserves the sparsity of the original fluid matrix.

Proof. Let $i, j \in \mathbb{N}$ be the indices of two fluid nodes which do not share the same edge (see Figure 2). We will show that its corresponding matrix entry in each block of (4.13) vanishes. The matrix associated with (4.13) has a diagonal block structure; for instance, in two dimensions we have

$$\mathbf{R}^n \stackrel{\text{def}}{=} \begin{bmatrix} (\mathbf{B}^n)^T \mathbf{M} \mathbf{B}^n & 0 \\ 0 & (\mathbf{B}^n)^T \mathbf{M} \mathbf{B}^n \end{bmatrix},$$

327 where $M \in \mathbb{R}^{N_h^s \times N_h^s}$ denotes the (scalar) lumped-mass matrix of the solid and $B^n \in$
 328 $\mathbb{R}^{N_h^s \times N_h^f}$ the (scalar) Lagrange interpolation matrix from the fluid mesh to the solid
 329 mesh of the current configuration $\phi_h^n(\Sigma)$. Therefore, it suffices to discuss only the
 330 diagonal blocks of R^n .



331 FIG. 2. The support of two fluid shape functions (in gray and in orange) intersected by the
 332 interface $\phi_h^n(\Sigma)$, where i and j do not share the same edge.

333 Since the lumped-mass matrix is diagonal, we have $M_{lk} = \alpha_l \delta_{lk}$, with $\alpha_l \in \mathbb{R}$ and
 334 δ_{lk} standing for the Kronecker delta. Let e_i, e_j be the canonical basis vectors of \mathbb{R}^{N^f}
 335 associated with the nodes i, j . We have

$$\begin{aligned}
 336 \quad & ((B^n)^T M B^n)_{ij} = (B^n e_i)^T M B^n e_j \\
 337 \quad & = \sum_l \left(\sum_k M_{lk} (B^n e_j)_k \right) (B^n e_i)_l = \sum_l \alpha_l (B^n e_j)_l (B^n e_i)_l = 0. \\
 338
 \end{aligned}$$

339 The last equality follows from the fact that, since the supports of the fluid nodes i
 340 and j do not intersect (see Figure 2), the vectors $B^n e_j$ and $B^n e_i$ do not have any
 341 common nonzero entry. This completes the proof. \square

342 Owing to the results of Lemmas 4.4 and 4.7, we introduce the following new
 343 solution procedure.

344 For $n \geq 1$,

- 345 1. Interface update: $\phi_h^n = \mathbf{I}_\Sigma + \mathbf{d}_h^{n-1}$.
- 346 2. Find $(\mathbf{u}_h^n, p_h^n) \in \mathbf{V}_h \times Q_h$ such that

$$\begin{aligned}
 347 \quad (4.14) \quad & \rho^f (\partial_\tau \mathbf{u}_h^n, \mathbf{v}_h)_\Omega + a_h^f(\mathbf{u}_h^{n-1}; (\mathbf{u}_h^n, p_h^n), (\mathbf{v}_h, q_h)) \\
 & + \frac{\rho^s \epsilon^s}{\tau} (\mathbf{B}_h(\mathbf{u}_h^n \circ \phi_h^n), \mathbf{B}_h(\mathbf{v}_h \circ \phi_h^n))_{\Sigma, h} \\
 348 \quad & = \frac{\rho^s \epsilon^s}{\tau} (\mathbf{d}_h^{n-1}, \mathbf{B}_h(\mathbf{v}_h \circ \phi_h^n))_{\Sigma, h} - a^s(\mathbf{d}_h^{n-1}, \mathbf{B}_h(\mathbf{v}_h \circ \phi_h^n))
 \end{aligned}$$

349 for all $(\mathbf{v}_h, q_h) \in \mathbf{V}_h \times Q_h$.

- 350 3. Find $\lambda_h^n \in \Lambda_h$ such that

$$\begin{aligned}
 351 \quad (4.15) \quad & b_h(\lambda_h^n, \mathbf{w}_h) = \frac{\rho^s \epsilon^s}{\tau} (\mathbf{B}_h(\mathbf{u}_h^n \circ \phi_h^n) - \dot{\mathbf{d}}_h^{n-1}, \mathbf{w}_h)_\Sigma + a^s(\mathbf{d}_h^{n-1}, \mathbf{w}_h) \\
 352
 \end{aligned}$$

353 for all $\mathbf{w}_h \in \mathbf{W}_h$.

- 354 4. Find $\dot{\mathbf{d}}_h^n \in \mathbf{W}_h$, with $\dot{\mathbf{d}}_h^n = \partial_\tau \mathbf{d}_h^n$, such that

$$\begin{aligned}
 355 \quad (4.16) \quad & \rho^s \epsilon^s (\partial_\tau \dot{\mathbf{d}}_h^n, \mathbf{w}_h)_{\Sigma, h} + a^s(\mathbf{d}_h^n, \mathbf{w}_h) = b_h(\lambda_h^n, \mathbf{w}_h) \\
 356
 \end{aligned}$$

357 for all $\mathbf{w}_h \in \mathbf{W}_h$.

358 From a practical point of view, it is worth noting that, using (4.16), the relations
 359 (4.14)–(4.15) can also be rewritten equivalently, by replacing the terms containing
 360 \mathbf{d}_h^{n-1} , as

$$\begin{aligned} & \rho^f (\partial_\tau \mathbf{u}_h^n, \mathbf{v}_h) + a_h^f(\mathbf{u}_h^{n-1}; (\mathbf{u}_h^n, p_h^n), (\mathbf{v}_h, q_h)) \\ & + \frac{\rho^s \epsilon^s}{\tau} (\mathbf{B}_h(\mathbf{u}_h^n \circ \phi_h^n), \mathbf{B}_h(\mathbf{v}_h \circ \phi_h^n))_{\Sigma, h} \\ & = \frac{\rho^s \epsilon^s}{\tau} (\dot{\mathbf{d}}_h^{n-1} + \tau \partial_\tau \dot{\mathbf{d}}_h^{n-1}, \mathbf{B}_h(\mathbf{v}_h \circ \phi_h^n))_{\Sigma, h} - b_h(\boldsymbol{\lambda}_h^{n-1}, \mathbf{B}_h(\mathbf{v}_h \circ \phi_h^n)) \end{aligned}$$

362 and

$$363 \quad b_h(\boldsymbol{\lambda}_h^n, \mathbf{w}_h) = \frac{\rho^s \epsilon^s}{\tau} (\mathbf{B}_h(\mathbf{u}_h^n \circ \phi_h^n) - \dot{\mathbf{d}}_h^{n-1} - \tau \partial_\tau \dot{\mathbf{d}}_h^{n-1}, \mathbf{w}_h)_{\Sigma, h} + b_h(\boldsymbol{\lambda}_h^{n-1}, \mathbf{w}_h)$$

364 for $n \geq 2$. The advantage of these expressions is that, since the solid elastic term has
 365 been eliminated, only solid velocities need to be transferred from the solid to the fluid
 366 (as in a standard Dirichlet–Neumann loosely coupled scheme). The resulting solution
 367 procedure is detailed in Algorithm 4.3.

368 *Remark 4.8.* It should be noted that Algorithm 4.3 requires $\boldsymbol{\lambda}_h^1, \dot{\mathbf{d}}_h^1$ as initial
 369 conditions, which can be obtained by performing the first step of (4.14)–(4.16). In
 370 the particular case in which $\mathbf{d}_h^0 = \dot{\mathbf{d}}_h^0 = \mathbf{0}$, we can start the time-stepping directly
 371 with Algorithm 4.3 for $n \geq 1$.

372 The computer implementation of Algorithm 4.3 is straightforward within a stan-
 373 dard finite element library. The algebraic formulation of the steps 2–4 are briefly
 374 discussed in the next paragraph.

Algorithm 4.3. Loosely coupled scheme.

For $n \geq 2$,

1. Interface update: $\phi_h^n = \mathbf{I}_\Sigma + \mathbf{d}_h^{n-1}$.
2. Fluid step: find $(\mathbf{u}_h^n, p_h^n) \in \mathbf{V}_h \times Q_h$ such that

$$\begin{aligned} & \rho^f (\partial_\tau \mathbf{u}_h^n, \mathbf{v}_h)_\Omega + a_h^f(\mathbf{u}_h^{n-1}; (\mathbf{u}_h^n, p_h^n), (\mathbf{v}_h, q_h)) \\ (4.17) \quad & + \frac{\rho^s \epsilon^s}{\tau} (\mathbf{B}_h(\mathbf{u}_h^n \circ \phi_h^n), \mathbf{B}_h(\mathbf{v}_h \circ \phi_h^n))_{\Sigma, h} \\ & = \frac{\rho^s \epsilon^s}{\tau} (2\dot{\mathbf{d}}_h^{n-1} - \dot{\mathbf{d}}_h^{n-2}, \mathbf{B}_h(\mathbf{v}_h \circ \phi_h^n))_{\Sigma, h} - b_h(\boldsymbol{\lambda}_h^{n-1}, \mathbf{B}_h(\mathbf{v}_h \circ \phi_h^n)) \end{aligned}$$

for all $(\mathbf{v}_h, q_h) \in \mathbf{V}_h \times Q_h$.

3. Evaluate fluid load: find $\boldsymbol{\lambda}_h^n \in \boldsymbol{\Lambda}_h$ such that

$$(4.18) \quad b_h(\boldsymbol{\lambda}_h^n, \mathbf{w}_h) = \frac{\rho^s \epsilon^s}{\tau} (\mathbf{B}_h(\mathbf{u}_h^n \circ \phi_h^n) - 2\dot{\mathbf{d}}_h^{n-1} + \dot{\mathbf{d}}_h^{n-2}, \mathbf{w}_h)_{\Sigma, h} + b_h(\boldsymbol{\lambda}_h^{n-1}, \mathbf{w}_h)$$

for all $\mathbf{w}_h \in \mathbf{W}_h$.

4. Solid step: find $\dot{\mathbf{d}}_h^n \in \mathbf{W}_h$, with $\dot{\mathbf{d}}_h^n = \partial_\tau \mathbf{d}_h^n$, such that

$$(4.19) \quad \rho^s \epsilon^s (\partial_\tau \dot{\mathbf{d}}_h^n, \mathbf{w}_h)_{\Sigma, h} + a^s(\dot{\mathbf{d}}_h^n, \mathbf{w}_h) = b_h(\boldsymbol{\lambda}_h^n, \mathbf{w}_h)$$

for all $\mathbf{w}_h \in \mathbf{W}_h$.

375 **4.2. Computer implementation.** Let \mathbf{u}^n , \mathbf{p}^n , \mathbf{d}^n , $\dot{\mathbf{d}}^n$, λ^n , and ϕ^n denote the
 376 arrays of degrees of freedom associated with \mathbf{u}_h^n , p_h^n , \mathbf{d}_h^n , $\dot{\mathbf{d}}_h^n$, λ_h^n , and ϕ_h^n , respectively.
 377 We also denote by \mathbf{x} the array of coordinates of the points of the triangulation \mathcal{T}_h^s .
 378 For the sake of clarity, we first consider the separated solution of the fluid without
 379 the coupling with the immersed solid. This yields the following type of linear system
 380 at each time-step:

$$381 \quad (4.20) \quad \begin{bmatrix} \mathbf{A}^f & \mathbf{C} \\ -\mathbf{C} & \mathbf{S} \end{bmatrix} \begin{bmatrix} \mathbf{u}^n \\ \mathbf{p}^n \end{bmatrix} = \begin{bmatrix} \mathbf{b}^{n-1} \\ 0 \end{bmatrix},$$

383 with the notation

$$384 \quad \mathbf{A}^f \stackrel{\text{def}}{=} \frac{\rho^f}{\tau} \mathbf{M}^f + \mathbf{K}^f, \quad \mathbf{b}^{n-1} \stackrel{\text{def}}{=} \frac{\rho^f}{\tau} \mathbf{M}^f \mathbf{u}^{n-1}.$$

385 Here, the matrices \mathbf{M}^f and $\begin{bmatrix} \mathbf{K}^f & \mathbf{C} \\ -\mathbf{C} & \mathbf{S} \end{bmatrix}$ denote the algebraic counterpart of the bilinear
 386 forms $(\mathbf{u}_h, \mathbf{v}_h^f)$ and $a_h^f(\mathbf{u}_h^{n-1}; (\mathbf{u}_h, \mathbf{v}_h), (\mathbf{v}_h^f, q_h))$, respectively. Similarly, without inter-
 387 action with the fluid, we get, for the solid, the following linear system

$$388 \quad (4.21) \quad \mathbf{A}^s \mathbf{d}^n = \mathbf{r}^{n-1},$$

390 with

$$391 \quad \mathbf{A}^s \stackrel{\text{def}}{=} \frac{\rho^s \epsilon^s}{\tau^2} \mathbf{M}^s + \mathbf{K}^e, \quad \mathbf{r}^{n-1} \stackrel{\text{def}}{=} \frac{\rho^s \epsilon^s}{\tau^2} \mathbf{M}^s (\mathbf{d}^{n-1} + \tau \dot{\mathbf{d}}^{n-1}), \quad \dot{\mathbf{d}}^n = \partial_\tau \mathbf{d}^n.$$

392 Here, the matrices \mathbf{M}^s and \mathbf{K}^s stand for the algebraic counterpart of the bilinear
 393 forms $(\dot{\mathbf{d}}_h, \mathbf{w}_h)_{\Sigma, h}$ and $a^s(\mathbf{d}_h, \mathbf{w}_h)$, respectively. Note that, due to the lumped mass
 394 approximation, the matrix \mathbf{M}^s is diagonal. Finally, we consider the matrices \mathbf{B}^n and
 395 \mathbf{R}^n introduced in the proof of Lemma 4.7 and define \mathbf{L}^n as the *fluid-to-solid* vector
 396 interpolation matrix, e.g., for $d = 2$ we have

$$397 \quad \mathbf{L}^n \stackrel{\text{def}}{=} \begin{bmatrix} \mathbf{B}^n & 0 \\ 0 & \mathbf{B}^n \end{bmatrix}.$$

398 Based on all these considerations, the steps of Algorithm 4.3 can be reformulated, in
 399 an algebraic fashion, as:

400 1. Set:

$$401 \quad \phi^n = \mathbf{x} + \mathbf{d}^{n-1}$$

402 and evaluate the interpolation matrix \mathbf{B}^n ;

403 2. Solve fluid with solid inertial contributions:

$$404 \quad (4.22) \quad \begin{bmatrix} \mathbf{A}^f + \frac{\rho^s \epsilon^s}{\tau} \mathbf{R}^n & \mathbf{C} \\ -\mathbf{C} & \mathbf{S} \end{bmatrix} \begin{bmatrix} \mathbf{u}^n \\ \mathbf{p}^n \end{bmatrix} = \begin{bmatrix} \mathbf{b}^{n-1} \\ 0 \end{bmatrix};$$

406 3. Set:

$$407 \quad \lambda^n = \frac{\rho^s \epsilon^s}{\tau} \mathbf{M}^s (\mathbf{L}^n \mathbf{u}^n - 2\dot{\mathbf{d}}^{n-1} + \dot{\mathbf{d}}^{n-2}) + \lambda^{n-1};$$

408 4. Solve solid:

$$409 \quad \mathbf{A}^s \mathbf{d}^n = \mathbf{r}^{n-1} + \lambda^n.$$

410 It is worth recalling that, owing to Lemma 4.7, the matrix of the system (4.22)
 411 preserves the sparse pattern of the original fluid matrix \mathbf{A}^f .

412 **4.3. Energy stability.** In this section, we assume that $a^s(\cdot, \cdot)$ is an inner product
 413 into \mathbf{W} . The associated solid energy norm is denoted by $\|\cdot\|_s \stackrel{\text{def}}{=} \sqrt{a^s(\cdot, \cdot)}$. We also
 414 introduce the discrete norm $\|\cdot\|_{\Sigma, h} \stackrel{\text{def}}{=} \sqrt{(\cdot, \cdot)_{\Sigma, h}}$. We shall consider the following
 415 discrete reconstruction of the elastic bilinear form a^s : for all $\mathbf{d}_h \in \mathbf{W}_h$, we define
 416 $\mathbf{L}_h^s \mathbf{d}_h \in \mathbf{W}_h$ such that

$$417 \quad (4.23) \quad (\mathbf{L}_h^s \mathbf{d}_h, \mathbf{w}_h)_{\Sigma, h} = a^s(\mathbf{d}_h, \mathbf{w}_h)$$

419 for all $\mathbf{w}_h \in \mathbf{W}_h$. Furthermore, we define the discrete energy at the time-step $n \geq 0$
 420 as

$$421 \quad E^n = \frac{\rho^f}{2} \|\mathbf{u}_h^n\|_{0, \Omega}^2 + \frac{\rho^s \epsilon^s}{2} \|\dot{\mathbf{d}}_h^n\|_{0, \Sigma}^2 + \frac{1}{2} \|\mathbf{d}_h^n\|_s^2.$$

422 We will use the symbol \lesssim to indicate an inequality written up to a multiplicative
 423 constant (independent of the physical and discretization parameters).

424 The next result establishes the unconditional energy stability of Algorithm 4.3.

425 **THEOREM 4.9.** *Let $\{(\mathbf{u}_h^n, p_h^n, \dot{\mathbf{d}}_h^n, \mathbf{d}_h^n)\}_{n \geq 1}$ be given by Algorithm 4.3, initialized as*
 426 *in Remark 4.8. The following energy estimate holds for $n \geq 1$:*

$$427 \quad (4.24) \quad E^n \lesssim E^0 + \tau^2 \|\dot{\mathbf{d}}_h^0\|_s^2 + \frac{\tau^2}{\rho^s \epsilon^s} \|\mathbf{L}_h^s \mathbf{d}_h^0\|_{0, \Sigma}^2.$$

429 *Proof.* From (4.15)–(4.16), we have

$$430 \quad (4.25) \quad \frac{\rho^s \epsilon^s}{\tau} (\dot{\mathbf{d}}_h^n - \mathbf{B}_h(\mathbf{u}_h^n \circ \phi_h^n), \mathbf{w}_h)_{\Sigma, h} + a^s(\mathbf{d}_h^n - \mathbf{d}_h^{n-1}, \mathbf{w}_h) = 0$$

432 for all $\mathbf{w}_h \in \mathbf{W}_h$. In particular, owing to (4.23), we have

$$433 \quad (4.26) \quad \mathbf{B}_h(\mathbf{u}_h^n \circ \phi_h^n) = \dot{\mathbf{d}}_h^n + \frac{\tau}{\rho^s \epsilon^s} \mathbf{L}_h^s (\mathbf{d}_h^n - \mathbf{d}_h^{n-1}).$$

435 On the other hand, by taking $\mathbf{w}_h = \mathbf{B}_h(\mathbf{v}_h \circ \phi_h^n)$ in (4.25) and by adding the resulting
 436 expression to (4.14), we get

$$437 \quad (4.27) \quad \rho^f (\partial_\tau \mathbf{u}_h^n, \mathbf{v}_h)_\Omega + a_h^f(\mathbf{u}_h^{n-1}; (\mathbf{u}_h^n, p_h^n), (\mathbf{v}_h, q_h)) \\ 438 \quad + \rho^s \epsilon^s (\partial_\tau \dot{\mathbf{d}}_h^n, \mathbf{B}_h(\mathbf{v}_h \circ \phi_h^n))_{\Sigma, h} + a^s(\mathbf{d}_h^n, \mathbf{B}_h(\mathbf{v}_h \circ \phi_h^n)) = 0$$

440 for all $(\mathbf{v}_h, q_h) \in \mathbf{V}_h \times Q_h$. By taking $(\mathbf{v}_h, q_h) = (\mathbf{u}_h^n, p_h^n)$ in this expression and using
 441 the fact that

$$442 \quad a_h^f(\mathbf{u}_h^{n-1}; (\mathbf{u}_h^n, p_h^n), (\mathbf{u}_h^n, p_h^n)) \geq 2\mu \|\epsilon(\mathbf{u}_h^n)\|_{0, \Omega}^2,$$

443 we get

$$444 \quad (4.28) \quad \frac{\rho^f}{2} \partial_\tau \|\mathbf{u}_h^n\|_{0, \Omega}^2 + 2\mu \|\epsilon(\mathbf{u}_h^n)\|_{0, \Omega}^2 \\ 445 \quad + \rho^s \epsilon^s (\partial_\tau \dot{\mathbf{d}}_h^n, \mathbf{B}_h(\mathbf{u}_h^n \circ \phi_h^n))_{\Sigma, h} + a^s(\mathbf{d}_h^n, \mathbf{B}_h(\mathbf{u}_h^n \circ \phi_h^n)) \leq 0.$$

447 We then proceed similarly to [20], by inserting (4.26) into (4.28). This yields

$$448 \quad (4.29) \quad \frac{\rho^f}{2} \partial_\tau \|\mathbf{u}_h^n\|_{0, \Omega}^2 + 2\mu \|\epsilon(\mathbf{u}_h^n)\|_{0, \Omega}^2 + \frac{\rho^s}{2} \partial_\tau \|\dot{\mathbf{d}}_h^n\|_{\Sigma, h}^2 + \frac{1}{2} \partial_\tau \|\mathbf{d}_h^n\|_s^2 \\ 449 \quad + \underbrace{\tau (\partial_\tau \dot{\mathbf{d}}_h^n, \mathbf{L}_h^s (\mathbf{d}_h^n - \mathbf{d}_h^{n-1}))_{\Sigma, h}}_{T_1} + \underbrace{\frac{\tau}{\rho^s \epsilon^s} a^s(\mathbf{d}_h^n, \mathbf{L}_h^s (\mathbf{d}_h^n - \mathbf{d}_h^{n-1}))}_{T_2} \leq 0.$$

451

452 It only remains to estimate the terms T_1 and T_2 . For the first term, using (4.23), we
453 have

$$454 \quad T_1 = \tau(\dot{\mathbf{d}}_h^n - \dot{\mathbf{d}}_h^{n-1}, \mathbf{L}_h^s \dot{\mathbf{d}}_h^n)_{\Sigma, h} = \tau a^s(\dot{\mathbf{d}}_h^n - \dot{\mathbf{d}}_h^{n-1}, \dot{\mathbf{d}}_h^n) \geq \frac{\tau}{2} (\|\dot{\mathbf{d}}_h^n\|_s^2 - \|\dot{\mathbf{d}}_h^{n-1}\|_s^2).$$

455 Finally, for the last term, we have

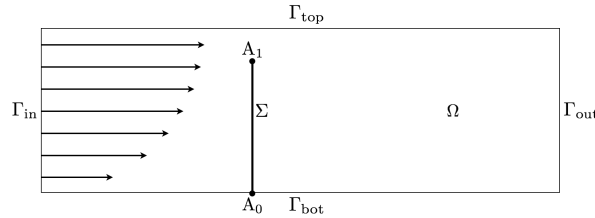
$$456 \quad T_2 = \frac{\tau}{\rho^s \epsilon^s} (\mathbf{L}_h^s \dot{\mathbf{d}}_h^n, \mathbf{L}_h^s (\mathbf{d}_h^n - \mathbf{d}_h^{n-1}))_{\Sigma, h} \geq \frac{\tau}{2\rho^s \epsilon^s} (\|\mathbf{L}_h^s \dot{\mathbf{d}}_h^n\|_{\Sigma, h}^2 - \|\mathbf{L}_h^s \dot{\mathbf{d}}_h^{n-1}\|_{\Sigma, h}^2).$$

457 We conclude by inserting the above two bounds into (4.29), by multiplying the re-
458 sulting expression by τ , by summing over n and by applying the norms equivalence
459 between $\|\cdot\|_{0, \Sigma}$ and $\|\cdot\|_{\Sigma, h}$ in \mathbf{W}_h , uniformly in h (see, e.g., [48, Chapter 15]). This
460 completes the proof. \square

461 **5. Numerical experiments.** The purpose of this section is to illustrate the per-
462 formance of Algorithm 4.3 via comparisons with the results provided by Algorithm 4.1
463 (with the regularized kinematic condition (4.2)) and by an alternative method recently
464 reported in the literature (see [1, Algorithm 4]). As the core motivation of the present
465 work is the efficient simulation of heart valves, two representative two-dimensional
466 examples which mimic the behavior of such systems in the open and closed configura-
467 tions, have been considered.

468 In what follows, a nonlinear Reissner–Mindlin beam model is considered for the
469 solid. Its spatial discretization is based on linear MITC (mixed interpolation of ten-
470 sorial components) elements, involving two displacements and one rotation as degrees
471 of freedom per node in the increments (see, e.g., [7]).

472 **5.1. Idealized valve without contact.** The first example is the heart-valve-
473 inspired benchmark problem considered in [29, 32, 50, 34, 12]. It consists of one
474 idealized valve modeled by a cantilevered elastic beam immersed in a two dimensional
475 channel filled with an incompressible Newtonian fluid, as shown in Figure 3. The
476 geometry of the fluid domain is given by $\Omega = [0, 8] \times [0, 0.805]$. The reference confi-
477 guration of the solid, Σ , is given by the segment whose endpoints are $A_0 = (2, 0)$ and
478 $A_1 = (2, 0.7)$ (see Figure 3). The physical parameters are, for the fluid, $\rho^f = 100$,
479 $\mu = 10$, and, for the solid, $\rho^s = 100$, $\epsilon^s = 0.0212$, with Young’s modulus $E = 5.6 \cdot 10^7$
480 and Poisson’s ratio $\nu = 0.4$.



481 FIG. 3. Geometric configuration of the first numerical example.

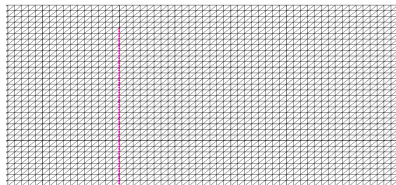
482 A no-slip boundary condition is enforced on Γ_{bot} , and a symmetry boundary
483 condition is imposed on Γ_{top} . Zero traction is enforced on the lateral boundary Γ_{out} ,
484 and the velocity is prescribed on Γ_{in} , as a half parabolic profile whose maximum
485 amplitude is defined by a positive time-dependent function $u_{\text{max}}(t)$, given by the
486 following expression:

$$487 \quad u_{\text{max}}(t) = 5(0.805)^2 (\sin(2\pi t) + 1.1), \quad t \in \mathbb{R}^+.$$

488 The solid is fully clamped at its bottom endpoint A_0 . Both the fluid and the solid are
 489 initially at rest. Considering the channel width of 0.805 as the characteristic length
 490 scale and the peak in flow speed of 6.8 as the characteristic flow speed, the associated
 491 Reynolds number is about 55.

492 In this first numerical example, in which no enclosed fluid is involved, we have
 493 observed that the grad-div stabilization has practically no impact on the quality of the
 494 numerical results. Hence, the free stabilization parameters in (3.5) have been set to
 495 $\lambda_M = 1$ and $\lambda_C = 0$ in both methods. The penalty parameter ε for Algorithm 4.1 in
 496 (4.2) is set to $\varepsilon = 10^{-5}$ (see [12]). We recall that Algorithm 4.3 does not involve any
 497 penalty parameter.

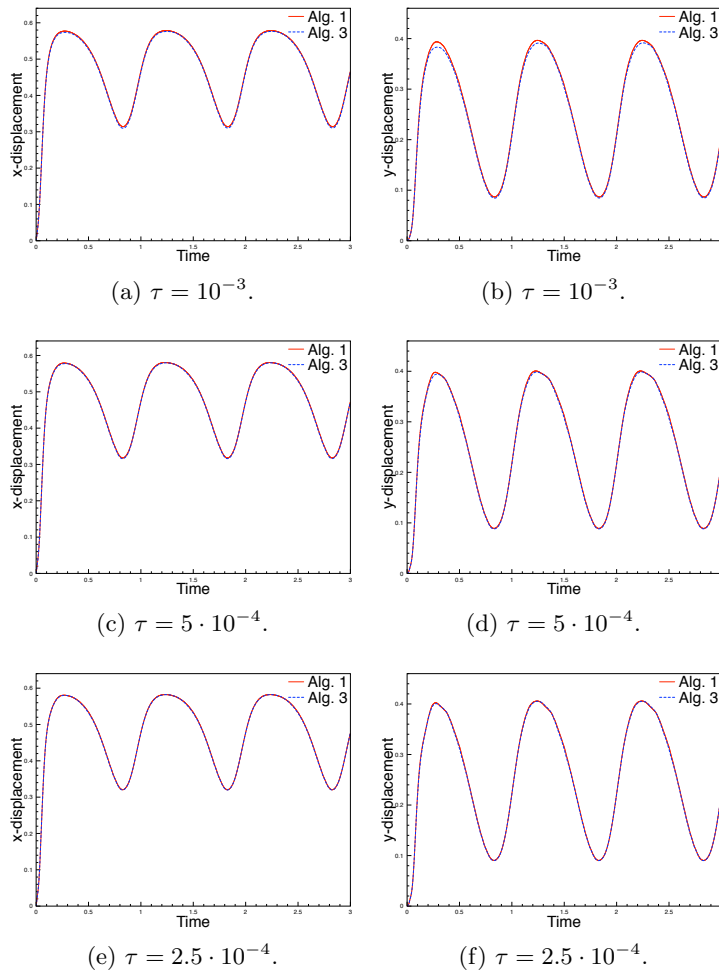
498 From the perturbed kinematic relation (4.26), Algorithms 4.1 and 4.3 are expected
 499 to deliver similar accuracy (up to the penalty error induced by ε in (4.2)) when the
 500 time-step length τ is sufficiently small. Hence, we propose to compare the results
 501 provided by these two methods, using three levels of time-step refinement given by
 502 $\tau \in \{(10^{-3}/2^i)\}_{i=0}^2$, and a fixed discretization in space based on a fluid mesh of
 503 16,384 triangles and a solid mesh of 64 segments (see Figure 4). Figure 5a, 5c, and
 504 5e present, respectively, for $i = \{0, 1, 2\}$, the comparison of the time history of the
 505 x -displacement of the solid at the upper tip A_1 , obtained with Algorithms 4.1 and
 506 4.3. Very close results are already obtained with the largest time-step $\tau = 10^{-3}$ (see
 507 Figure 5a). The agreement still improves when the time-step is refined. Note that the
 508 two curves become practically indistinguishable for the finest time grid $\tau = 2.5 \cdot 10^{-4}$
 509 (see Figure 5e). Similar observations can be made from Figures 5b, 5d, and 5f, which
 510 present the results for the y -displacement, respectively, for $i = \{0, 1, 2\}$. A slight
 511 difference is observed between the two curves for the largest time-step $\tau = 10^{-3}$ (see
 512 Figure 5b). Nevertheless, this discrepancy practically disappears in the next level of
 513 refinement (see Figure 5d).



514 FIG. 4. Zoom on the fluid and solid meshes.

519 For illustration purposes we have reported in Figure 6 some snapshots of the in-
 520 terface location and of the fluid velocity magnitude near the solid obtained at different
 521 time instants with Algorithms 4.1 and 4.3 for $\tau = 10^{-3}$. The very good agreement
 522 between both numerical approximations is noticeable. Similar observation can be in-
 523 ferred from the elevated pressure reported in Figure 7, obtained with $\tau = 10^{-3}$. As
 524 before, Algorithm 4.3 delivers practically the same results as Algorithm 4.1, predicting
 525 the similar shape of the pressure jump across the leaflet.

526 *Computational considerations.* We finally comment on the relative efficiency of
 527 the two methods. By construction, Algorithm 4.3 requires only 1 single fluid and solid
 528 evaluations per time-step. The efficiency of Algorithm 4.1 depends on the type of
 529 solution procedure for the coupled system (4.3). In the present study, this system has
 530 been solved via a Dirichlet–Neumann interface Newton-GMRES partitioned iterative
 531 method, which requires an average of 3 fluid and solid evaluations and 21 tangent
 532 fluid and solid evaluations per time-step. Note also that the conditioning of these
 533 fluid systems is worse than in Algorithm 4.3 due to the penalized treatment of the



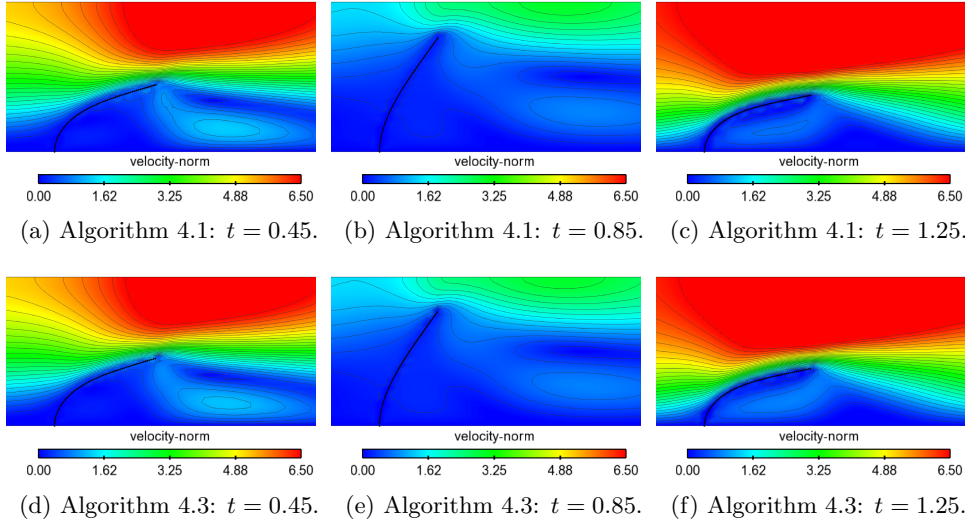
515 FIG. 5. *Time history of the displacement of solid at the upper tip A_1 obtained with Algo-*
 516 *gorithms 4.1 and 4.3. Left column: x -displacement. Right column: y -displacement.*

534 interface coupling. This clearly points out the advantages of Algorithm 4.3 in terms
 535 of computational cost.

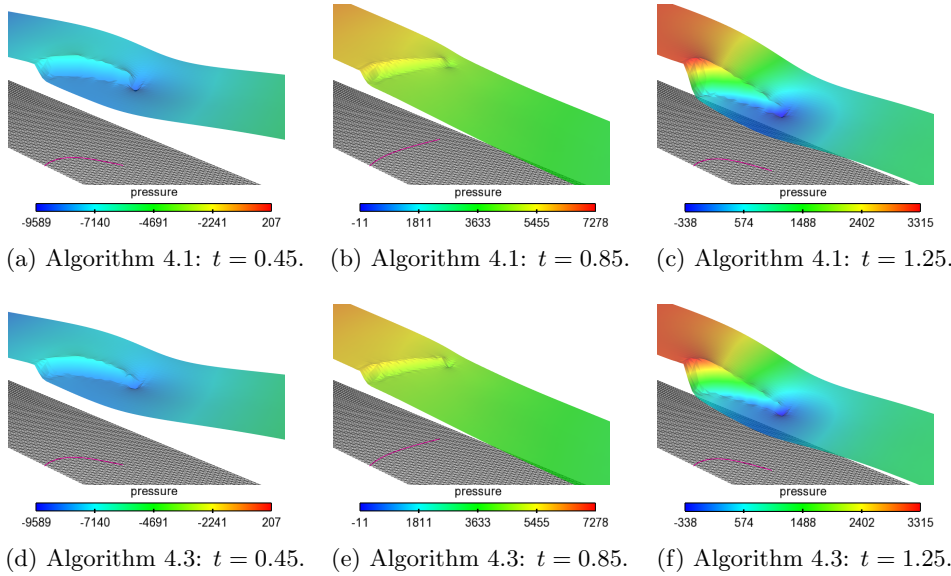
537 **5.2. Idealized valve with contact.** As a second example, we consider an ex-
 538 tension of the previous one in which the idealized valve is now long enough to get
 539 into contact with the upper wall, as shown in Figure 8. The geometry of the fluid
 540 domain is given by $\Omega = [0, 8] \times [0, 0.805]$ as in the previous example. The reference
 541 configuration of the solid, Σ , is defined by the following analytical expression:

$$542 \quad y(x) = \frac{1}{2} \sqrt{1 - \frac{(x - 11/2)^2}{(3/2)^2}}, \quad x \in [4, 5.112].$$

543 The coordinates of its endpoints, A_0 and A_1 , are then $(4, 0)$ and $(5.112, 0.483)$, re-
 544 spectively. The physical parameters for the fluid are $\rho^f = 1$ and $\mu = 0.03$. For the
 545 solid, we have $\rho^s = 1.2$, $\epsilon^s = 0.065$, with Young's modulus $E = 10^7$ and Poisson's
 546 ratio $\nu = 0.4$.



517 FIG. 6. Snapshots of the fluid velocity magnitude obtained with Algorithms 4.1 and 4.3.



518 FIG. 7. Snapshots of the fluid elevated pressure obtained with Algorithms 4.1 and 4.3.

547 A no-slip boundary condition is enforced on Γ_{bot} while a symmetry boundary
 548 condition is imposed on Γ_{top} . Zero traction is enforced on the lateral boundary Γ_{out} ,
 549 while on Γ_{in} , traction is imposed in terms of the following time-dependent pressure
 550 data $p_{\text{in}}(t)$:

$$551 \quad (5.1) \quad p_{\text{in}}(t) = \begin{cases} -200 \operatorname{atanh}(100t) & \text{if } 0 < t < 0.7, \\ 200 & \text{if } t \geq 0.7. \end{cases}$$

552

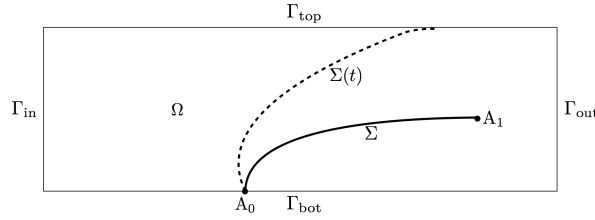


FIG. 8. Geometric configuration of the second numerical example.

The contact condition of the solid with the upper wall Γ_{top} is the following:

$$(5.2) \quad \mathbf{d} \cdot \mathbf{n}_{\Gamma_{\text{top}}} - g \leq 0 \quad \text{on } \Sigma,$$

where $\mathbf{n}_{\Gamma_{\text{top}}}$ denotes the (constant) exterior unit normal to Γ_{top} and $g : \Sigma \rightarrow \mathbb{R}^+$ stands for the gap function between Σ and Γ_{top} . At the discrete level, the inequality constraint (5.2) is approximated via a penalty method (see, e.g., [46]). This amounts to include, in $a^s(\mathbf{d}_h^n, \mathbf{w}_h)$, the following additional nonlinear term

$$(5.3) \quad \frac{\gamma_c E \epsilon^s}{h^2} ([\mathbf{d}_h^n \cdot \mathbf{n}_{\Gamma_{\text{top}}} - g + \epsilon_h]_+, \mathbf{w}_h)_{\Sigma},$$

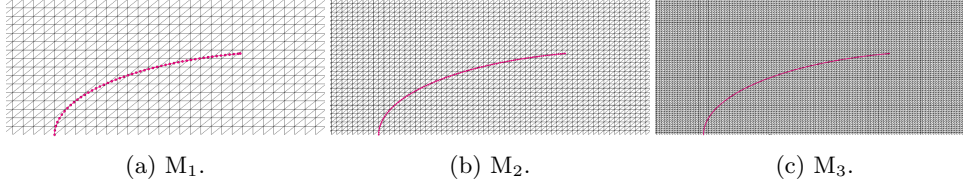
where $[x]_+ \stackrel{\text{def}}{=} \max\{0, x\}$, $\gamma_c > 0$ is a (dimensionless) user-defined parameter and $\epsilon_h > 0$ is a contact tolerance aimed at preventing penetration. In the results presented below, we have taken $\epsilon_h = \mathcal{O}(h)$ and $\gamma_c = 5 \cdot 10^{-3}$.

The fluid and the solid are initially at rest. The beam is pinched at A_0 (i.e, the rotation degree of freedom is free). We consider the channel width of 0.805 as the characteristic length scale. For the characteristic flow speed, we consider the typical values of 4 and 10, for the closing and opening phases, respectively. The associated Reynolds number is then approximately 107 and 268.

Numerical evidence (not reported here) indicates that the quality of the approximations provided by Algorithm 4.1 with the regularized kinematic condition (4.2), for this specific example with contact, is extremely sensitive to the penalty parameter ϵ . In order to circumvent these difficulties, we propose to consider as the reference solution the strongly coupled Nitsche-XFEM unfitted mesh approach reported in [1, Algorithm 4]. This method has multiple interesting features (e.g., Lagrange multipliers free, consistent treatment of the interface coupling, optimal error estimates, etc.) and is known to deliver superior spatial accuracy with respect to Algorithm 4.1 (see [12]). Nevertheless, the price to pay is an increased computational complexity and a much more involved computer implementation (careful track of the interface intersections, dynamic matrix pattern, etc.) with respect to Algorithms 4.1 and 4.3.

The accuracy of Algorithm 4.3 will be then evaluated with respect to the Nitsche-XFEM method, by considering three successive levels of grid refinement in space and time. The coarsest level, which will be referred to as M_1 , corresponds to a fluid mesh of 4,096 triangles. The solid mesh is made of 25 and 50 segments, respectively, for Nitsche-XFEM and Algorithm 4.3. The corresponding time-step is set to $\tau = 2 \cdot 10^{-3}$ and the contact tolerance in (5.3) to $\epsilon_h = 0.02$. The two subsequent space-time grids, denoted by M_2 and M_3 , are uniform refinements of M_1 with, respectively, a factor of 2 and 4 along both spatial and temporal directions. The three sets of fluid and solid meshes are shown in Figure 9. For Algorithm 4.3, the value of the user-defined parameter ϵ_M , in the SUPG/PSPG stabilization with enhanced interfacial

591 mass conservation (3.6), is set to 10^{-4} in all levels of refinement. For the Nitsche-
 592 XFEM method, the user-defined parameters are set to $\gamma = 100$, $\gamma_g = 1$ and $\gamma_v =$
 593 $\gamma_p = 0.01$, as detailed in [1, 12].



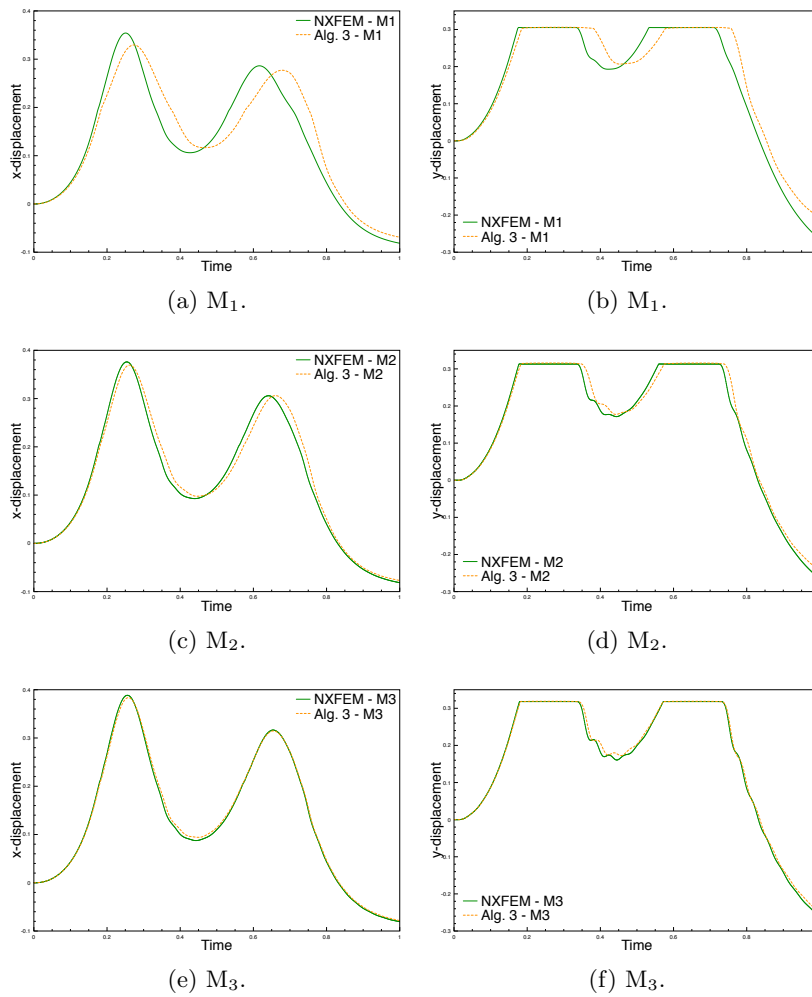
594 FIG. 9. Zoom on the fluid and solid meshes for the different levels of refinement.

595 As the negative prescribed pressure (5.1) builds up, the solid starts to bend and
 596 collides with Γ_{top} after some time instants. Due to the flexible nature of the structure,
 597 it is free to slide or even to bounce on the wall. When contact is occurring, the fluid
 598 velocity vanishes and a pressure jump across the interface is observed. Finally, after
 599 $t = 0.7$, a positive pressure builds up and the valve opens again. Figure 10 reports a
 600 comparison of the time history of the displacement of the solid at the upper tip A_1
 601 obtained with Nitsche-XFEM and Algorithm 4.3 for the three levels of refinement.
 602 The left and right columns show, respectively, the horizontal and vertical components
 603 of the displacement. Note that the flat part of the curves in the vertical displacement
 604 correspond to instants where contact occurs. The part of the curve between the two
 605 successive flat parts corresponds to the bouncing of the leaflet, illustrating the com-
 606 plex dynamics of the problem. A significant phase shift is observed between the two
 607 approximations for the coarsest level M_1 , but this discrepancy decreases with refine-
 608 ment. A better agreement is finally observed for the space-time grids M_2 and M_3 .

609 For illustration purposes, Figure 11 presents the interface location and the fluid
 610 velocity magnitude near the leaflet obtained at $t = 0.7$, for the three levels of refine-
 611 ment, with Nitsche-XFEM and Algorithm 4.3. Overall, a good agreement of the
 612 velocity field is already observed for the intermediate level M_2 (see Figure 11b and
 613 11e). Once more, this agreement improves with space-time grid refinement as Figure
 614 11c and 11f depict practically the same velocity field. The snapshots of the elevated
 615 pressure are given in Figure 12. The mismatch observed in Figure 10 with the coarsest
 616 approximation is clearly pointed out here in terms of the pressure jump (see Figure 12a
 617 and 12d). Note that these pressure jumps are not evaluated at the same interface
 618 location, even if evaluated at the same instant, which explains the mismatch. The
 619 situation improves via space-time grid refinement as we can infer from Figure 12c and
 620 12f, where the interface locations are now practically the same.

621 Finally, in order to provide a quantitative comparison of the two approaches, we
 622 evaluate the magnitude of the error between the two methods by measuring the L^2 -
 623 difference of the interface displacement for the three levels of refinement, as shown in
 624 Table 1. The results clearly show convergence after grid refinement.

625 *Computational considerations.* The benefits of Algorithm 4.3, with respect to the
 626 Nitsche-XFEM method considered in this example, are striking in terms of computa-
 627 tional complexity and computer implementation. Among them, it is worth mentioning
 628 the following: there is no mesh intersection (i.e., only localization of the solid nodes
 629 within the fluid mesh are needed) and no cut-FEM (i.e., the fluid equations are in-
 630 tegrated in the whole computational domain), the fluid system matrix has both a
 fixed size and a fixed standard pattern and, last but not least, the coupling scheme

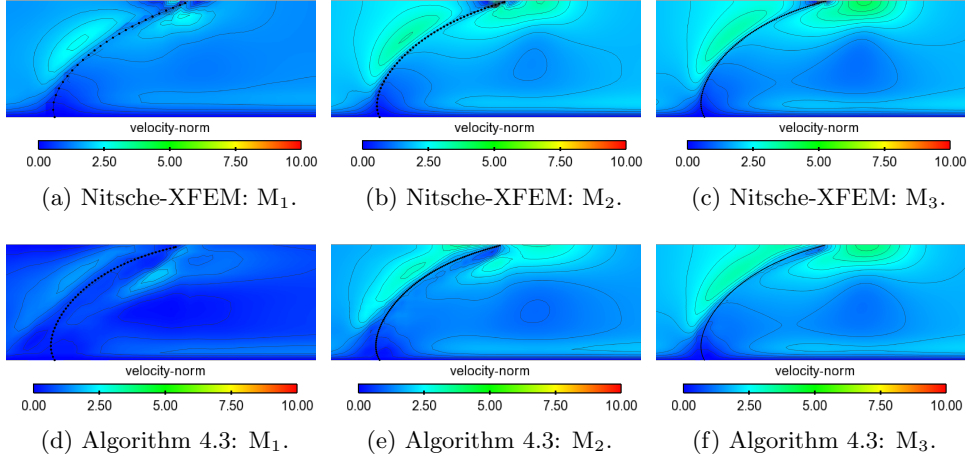


635 FIG. 10. Time history of the displacement of the solid at the upper tip A_1 obtained with
 636 Nitsche-XFEM and Algorithm 4.3. Left column: x -displacement. Right column: y -displacement.

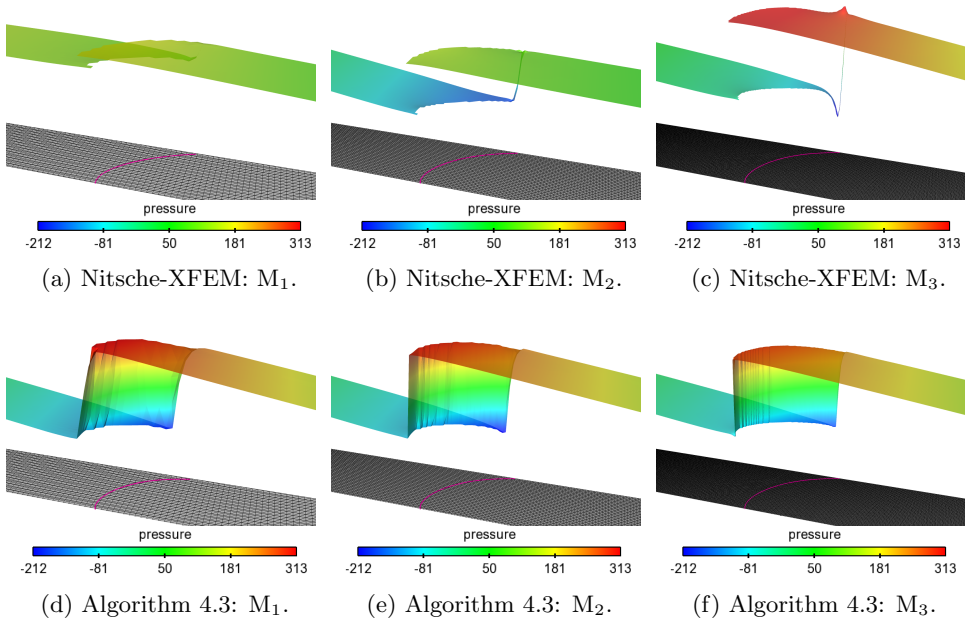
631 is loosely coupled. These advantages should however be pondered carefully, since
 632 the spatial accuracy of Algorithm 4.3 relies on the use of the penalty grad-div term
 633 (3.5)–(3.6), which can compromise the efficiency of the fluid solver, particularly in
 634 three-dimensional simulations (see [34, 16, 35]).

641 **6. Conclusions.** In this paper, we have introduced a new loosely coupled scheme
 642 for the numerical approximations of incompressible fluid-structure interaction prob-
 643 lems involving immersed thin-walled structures. The key ingredients of the proposed
 644 method are the following:

- 645 • Unfitted meshes and fictitious domain approximations in space (equivalent to
 646 a collocation method);
- 647 • Implicit treatment of the solid inertial effects within the fluid and explicit
 648 treatment of the elastic contribution;
- 649 • Lumped mass approximation in the solid.



637 FIG. 11. Snapshots of the fluid velocity magnitude at $t = 0.7$ obtained with Nitsche-XFEM and
638 Algorithm 4.3.



639 FIG. 12. Snapshots of the fluid elevated pressure at $t = 0.7$ obtained with Nitsche-XFEM and
640 Algorithm 4.3.

650 TABLE 1
651 L^2 -difference of the displacements approximations provided by Nitsche-XFEM and Algorithm 4.3.

Space-time grid	L^2 -difference
M_1	$3.18 \cdot 10^{-3}$
M_2	$7.48 \cdot 10^{-4}$
M_3	$1.61 \cdot 10^{-5}$

A salient feature of the resulting method is that it preserves both the size and the sparsity pattern of the original fluid matrix, while enabling a full splitting between the fluid and the solid time-marchings without compromising stability (Theorem 4.9). The splitting is parameter free and circumvents the usual ill-conditioning issues of fictitious domain methods involving penalized approximations of the kinematic coupling. The numerical evidence of section 5 confirmed these findings and highlighted a very good performance, in terms of accuracy and robustness, with respect to strongly coupled unfitted mesh approaches that are known to be much more computationally onerous.

The main limitation of the present numerical method comes from the spatial discretization, whose accuracy relies on a grad-div penalty term that enhances mass conservation at the expense of spoiling the conditioning of the fluid system. A forthcoming extension of this work will address the combination of the proposed loosely coupled scheme with alternative enhanced interfacial mass conservation techniques which avoid this ill-conditioning issue. Another important problem, not addressed in the present work, is the case of the coupling with immersed thick-walled solids. A first attempt in this direction could be to combine the arguments of this work with the ideas from [26, 11]. This is a particularly difficult problem, because the thick-walled nature of the solid is expected to harm the optimality of the time splitting error, as in the case of fitted meshes (see [26, 24]).

REFERENCES

- [1] F. ALAUZET, B. FABRÈGES, M. A. FERNÁNDEZ, AND M. LANDAJUELA, *Nitsche-XFEM for the coupling of an incompressible fluid with immersed thin-walled structures*, *Comput. Methods Appl. Mech. Engrg.*, 301 (2016), pp. 300–335.
- [2] M. ANNESE, *Time integration schemes for fluid-structure interaction problems: Non-fitted FEMs for immersed thin structures*, PhD thesis, Università degli studi di Brescia, 2017.
- [3] M. ASTORINO, J.-F. GERBEAU, O. PANTZ, AND K.-F. TRAORÉ, *Fluid-structure interaction and multi-body contact: Application to aortic valves*, *Comput. Methods Appl. Mech. Engrg.*, 198 (2009), pp. 3603–3612.
- [4] F. BAALJENS, *A fictitious domain/mortar element method for fluid-structure interaction*, *Int. J. Numer. Methods Fluids*, 35 (2001), pp. 743–761.
- [5] S. BADIA, A. QUAINI, AND A. QUARTERONI, *Splitting methods based on algebraic factorization for fluid-structure interaction*, *SIAM J. Sci. Comput.*, 30 (2008), pp. 1778–1805.
- [6] J. BANKS, W. HENSHAW, AND D. SCHWENDEMAN, *An analysis of a new stable partitioned algorithm for FSI problems. Part II: Incompressible flow and structural shells*, *J. Comput. Phys.*, 268 (2014), pp. 399–416.
- [7] K. BATHE, *Finite Element Procedures*, Prentice Hall, Englewood Cliffs, NJ, 1996.
- [8] F. BERTRAND, P. A. TANGUY, AND F. THIBAUT, *A three-dimensional fictitious domain method for incompressible fluid flow problems*, *Int. J. Numer. Methods Fluids*, 25 (1997), pp. 719–736.
- [9] D. BOFFI, N. CAVALLINI, AND L. GASTALDI, *Finite element approach to immersed boundary method with different fluid and solid densities*, *Math. Models Methods Appl. Sci.*, 21 (2011), pp. 2523–2550.
- [10] D. BOFFI, N. CAVALLINI, AND L. GASTALDI, *The finite element immersed boundary method with distributed Lagrange multiplier*, *SIAM J. Numer. Anal.*, 53 (2015), pp. 2584–2604.
- [11] D. BOFFI AND L. GASTALDI, *A fictitious domain approach with lagrange multiplier for fluid-structure interactions*, *Numer. Math.*, 135 (2017), pp. 711–732.
- [12] L. BOILEVIN-KAYL, M. A. FERNÁNDEZ, AND J.-F. GERBEAU, *Numerical methods for immersed FSI with thin-walled structures*, *Comput. Fluids*, (2018), doi:10.1016/j.compfluid.2018.05.024.
- [13] M. BUKAC, C. CANIC, R. GLOWINSKI, T. TAMBACA, AND A. QUAINI, *Fluid-structure interaction in blood flow capturing non-zero longitudinal structure displacement*, *J. Comp. Phys.*, 235 (2013), pp. 515–541.
- [14] E. BURMAN AND M. A. FERNÁNDEZ, *Stabilization of explicit coupling in fluid-structure interaction involving fluid incompressibility*, *Comput. Methods Appl. Mech. Engrg.*, 198 (2009), pp. 766–784.

- 707 [15] E. BURMAN AND M. A. FERNÁNDEZ, *An unfitted Nitsche method for incompressible fluid-*
708 *structure interaction using overlapping meshes*, *Comput. Methods Appl. Mech. Engrg.*,
709 279 (2014), pp. 497–514.
- 710 [16] H. CASQUERO, C. BONA-CASAS, AND H. GOMEZ, *NURBS-based numerical proxies for red blood*
711 *cells and circulating tumor cells in microscale blood flow*, *Comput. Methods Appl. Mech.*
712 *Engrg.*, 316 (2017), pp. 646–667.
- 713 [17] P. CAUSIN, J.-F. GERBEAU, AND F. NOBILE, *Added-mass effect in the design of partitioned*
714 *algorithms for fluid-structure problems*, *Comput. Methods Appl. Mech. Engrg.*, 194 (2005),
715 pp. 4506–4527.
- 716 [18] N. DINIZ DOS SANTOS, J.-F. GERBEAU, AND J.-F. BOURGAT, *A partitioned fluid-structure al-*
717 *gorithm for elastic thin valves with contact*, *Comput. Methods Appl. Mech. Engrg.*, 197
718 (2008), pp. 1750–1761.
- 719 [19] B. FABRÈGES AND B. MAURY, *Approximation of single layer distributions by dirac masses in*
720 *finite element computations*, *J. Sci. Comput.*, 58 (2014), pp. 25–40.
- 721 [20] M. A. FERNÁNDEZ, *Incremental displacement-correction schemes for incompressible fluid-*
722 *structure interaction: stability and convergence analysis*, *Numer. Math.*, 123 (2013),
723 pp. 21–65.
- 724 [21] M. A. FERNÁNDEZ, J. GERBEAU, AND C. GRANDMONT, *A projection semi-implicit scheme for*
725 *the coupling of an elastic structure with an incompressible fluid*, *Int. J. Numer. Methods*
726 *Engrg.*, 69 (2007), pp. 794–821.
- 727 [22] M. A. FERNÁNDEZ AND M. LANDAJUELA, *Splitting schemes for incompressible fluid/thin-walled*
728 *structure interaction with unfitted meshes*, *C. R. Math. Acad. Sci. Paris*, 353 (2015),
729 pp. 647–652.
- 730 [23] M. A. FERNÁNDEZ, M. LANDAJUELA, AND M. VIDRASCU, *Fully decoupled time-marching*
731 *schemes for incompressible fluid/thin-walled structure interaction*, *J. Comput. Phys.*, 297
732 (2015), pp. 156–181.
- 733 [24] M. A. FERNÁNDEZ AND J. MULLAERT, *Convergence and error analysis for a class of split-*
734 *ting schemes in incompressible fluid-structure interaction*, *J. Numer. Anal.*, 36 (2016),
735 pp. 1748–1782.
- 736 [25] M. A. FERNÁNDEZ, J. MULLAERT, AND M. VIDRASCU, *Explicit Robin-Neumann schemes for*
737 *the coupling of incompressible fluids with thin-walled structures*, *Comput. Methods Appl.*
738 *Mech. Engrg.*, 267 (2013), pp. 566–593.
- 739 [26] M. A. FERNÁNDEZ, J. MULLAERT, AND M. VIDRASCU, *Generalized Robin-Neumann explicit*
740 *coupling schemes for incompressible fluid-structure interaction: Stability analysis and*
741 *numerics*, *Int. J. Numer. Methods Engrg.*, 101 (2015), pp. 199–229.
- 742 [27] C. FÖRSTER, W. WALL, AND E. RAMM, *Artificial added mass instabilities in sequential staggered*
743 *coupling of nonlinear structures and incompressible viscous flows*, *Comput. Methods Appl.*
744 *Mech. Engrg.*, 196 (2007), pp. 1278–1293.
- 745 [28] A. GERSTENBERGER AND W. WALL, *An extended finite element method/Lagrange multiplier*
746 *based approach for fluid-structure interaction*, *Comput. Methods Appl. Mech. Engrg.*, 197
747 (2008), pp. 1699–1714.
- 748 [29] A. J. GIL, A. ARRANZ CARREÑO, J. BONET, AND O. HASSAN, *An enhanced Immersed Structural*
749 *Potential Method for fluid-structure interaction*, *J. Comput. Phys.*, 250 (2013),
750 pp. 178–205.
- 751 [30] R. GLOWINSKI, T. PAN, T. HESLA, AND D. JOSEPH, *A distributed Lagrange multiplier/fictitious*
752 *domain method for particulate flows*, *Int. J. Multiphase Flow*, 25 (1999), pp. 755–794.
- 753 [31] G. GUIDOBONI, R. GLOWINSKI, N. CAVALLINI, AND S. CANIC, *Stable loosely-coupled-type*
754 *algorithm for fluid-structure interaction in blood flow*, *J. Comp. Phys.*, 228 (2009),
755 pp. 6916–6937.
- 756 [32] C. HESCH, A. J. GIL, A. ARRANZ CARREÑO, AND J. BONET, *On continuum immersed strategies*
757 *for Fluid-Structure Interaction*, *Comput. Methods Appl. Mech. Engrg.*, 247–248 (2012),
758 pp. 51–64.
- 759 [33] C. KADAPA, W. DETTMER, AND D. PERIĆ, *A stabilised immersed framework on hierarchi-*
760 *cal b-spline grids for fluid-flexible structure interaction with solid-solid contact*, *Comput.*
761 *Methods Appl. Mech. Engrg.*, 335 (2018), pp. 472–489.
- 762 [34] D. KAMENSKY, M.-C. HSU, D. SCHILLINGER, J. EVANS, A. AGGARWAL, Y. BAZILEVS, M. SACKS,
763 AND T. HUGHES, *An immersogeometric variational framework for fluid-structure interac-*
764 *tion: Application to bioprosthetic heart valves*, *Comput. Methods Appl. Mech. Engrg.*, 284
765 (2015), pp. 1005–1053.
- 766 [35] D. KAMENSKY, Y. HSU, M.-C. DND YU, E. J. A., M. SACKS, AND T. HUGHES, *Immersogeometric*
767 *cardiovascular fluid-structure interaction analysis with divergence-conforming B-splines*,
768 *Comput. Methods Appl. Mech. Engrg.*, 314 (2017), pp. 408–472.

- 769 [36] W. KIM AND H. LEE, I. CHOI, *A weak-coupling immersed boundary method for fluidstructure*
770 *interaction with low density ratio of solid to fluid*, J. Comput. Phys., 359 (2018),
771 pp. 296–311.
- 772 [37] M. LANDAJUELA, M. VIDRASCU, D. CHAPELLE, AND M. A. FERNÁNDEZ, *Coupling schemes for*
773 *the FSI forward prediction challenge: Comparative study and validation*, Int. J. Numer.
774 Methods Biomed. Engrg., 33 (2017), e02813, 23.
- 775 [38] M. LANDAJUELA, M. VIDRASCU, D. CHAPELLE, AND M. A. FERNÁNDEZ, *Coupling schemes for*
776 *the FSI forward prediction challenge: comparative study and validation*, Int. J. Numer.
777 Methods Biomed. Engrg., 33 (2017), e2813.
- 778 [39] P. LE TALLEC AND J. MOURO, *Fluid structure interaction with large structural displacements*,
779 Comput. Methods Appl. Mech. Engrg., 190 (2001), pp. 3039–3067.
- 780 [40] A. LEGAY, J. CHESSA, AND T. BELYTSCHKO, *An Eulerian-Lagrangian method for fluid-*
781 *structure interaction based on level sets*, Comput. Methods Appl. Mech. Engrg., 195 (2006),
782 pp. 2070–2087.
- 783 [41] F. NOBILE AND C. VERGARA, *An effective fluid-structure interaction formulation for vascular*
784 *dynamics by generalized Robin conditions*, SIAM J. Sci. Comput., 30 (2008), pp. 731–763.
- 785 [42] A. PATEL, *Lagrange multiplier method with penalty for elliptic and parabolic interface problems*,
786 J. Appl. Math. Comput., 37 (2011), pp. 37–56.
- 787 [43] C. PESKIN, *The immersed boundary method*, Acta Numer., 11 (2002), pp. 479–517.
- 788 [44] A. QUAINI AND A. QUARTERONI, *A semi-implicit approach for fluid-structure interaction based*
789 *on an algebraic fractional step method*, Math. Models Methods Appl. Sci., 17 (2007),
790 pp. 957–983.
- 791 [45] T. SAWADA AND A. TEZUKA, *LLM and X-FEM based interface modeling of fluid-thin structure*
792 *interactions on a non-interface-fitted mesh*, Comput. Mech., 48 (2011), pp. 319–332.
- 793 [46] R. SCHOLZ, *Numerical solution of the obstacle problem by the penalty method*, Computing, 32
794 (1984), pp. 297–306.
- 795 [47] T. TEZDUYAR, *Stabilized finite element formulations for incompressible flow computations*, in
796 Advances in Applied Mechanics, vol. 28, Academic Press, Boston, 1992, pp. 1–44.
- 797 [48] V. THOMÉE, *Galerkin finite element methods for parabolic problems*, Springer Series in Com-
798 putational Mathematics 25, second ed., Springer, Berlin, 2006.
- 799 [49] E. VAN BRUMMELEN, *Added mass effects of compressible and incompressible flows in fluid-*
800 *structure interaction*, J. Appl. Mech., 76 (2009), 021206–7.
- 801 [50] T. WICK, *Flapping and contact FSI computations with the fluid-solid interface-*
802 *tracking/interface-capturing technique and mesh adaptivity*, Comput. Mech., 53 (2014),
803 pp. 29–43.
- 804 [51] A. ZILIAN AND A. LEGAY, *The enriched space-time finite element method (EST) for simulta-*
805 *neous solution of fluid-structure interaction*, Int. J. Numer. Methods Engrg., 75 (2008),
806 pp. 305–334.